UNIVERSIDAD TÉCNICA FEDERICO SANTA MARÍA

DEPARTAMENTO DE FÍSICA

The Evolution of the Spin Alignments of Dark Matter Halos in the Cosmic Web

David Tobar Moncada

Submitted in partial fulfillment of the requirements for the degree of
Master of Science mention in Physics.

Advisor: Dr. Antonio Montero-Dorta
Co-advisor: Dr. Rory Smith

March 24, 2026

CONSTANCIA DE VALIDACIÓN Y CONFIDENCIALIDAD DE MONOGRAFÍA A REPOSITORIO ACADÉMICO

1.- IDENTIFICACIÓN DEL TRABAJO ACADÉMICO

Tipo de monografía (marcar una opción): ☐ Memoria o trabajo de título ■ Tesis de Postgrado

Título del trabajo: **The Evolution of Spin Alignments of Dark Matter Halos in the Cosmic Web**

Nombre del candidato(a): **David Antonio Tobar Moncada**

Carrera / Grado: Magíster en Ciencias, mención en Física

Campus: San Joaquín

Departamento: Física

2.- VALIDACIÓN DEL PROFESOR GUÍA/DIRECTOR DE TESIS

Yo, **Antonio David Montero Dorta**, en mi calidad de profesor(a) guía/director(a) del trabajo académico mencionado anteriormente **DEJO CONSTANCIA** que:

- He revisado esta versión del documento y corresponde a la versión final aprobada del trabajo.
- El trabajo cumple con los requisitos académicos y de formato establecidos por la institución.

3.- EVALUACIÓN DE CONFIDENCIALIDAD POR PROPIEDAD INDUSTRIAL (marcar una opción)

■ El trabajo **NO contiene** información que amerite confidencialidad y puede ser publicado de inmediato en repositorio con acceso abierto.

☐ El trabajo **CONTIENE** información con potenciales implicancias de propiedad industrial o intelectual y requiere un periodo de confidencialidad (**embargo**) por **(marcar una opción)**:

☐ 6 meses ☐ 12 meses ☐ 2 años ☐ 3 años ☐ 5 años ☐ 10 años

Fundamentación de la necesidad de confidencialidad (obligatorio si se solicita embargo):

4.- FIRMAS

Profesor(a) guía o director(a) de memoria o tesis:

Fecha: 17 de marzo de 2026 **Firma:**

Estudiante o Candidato(a):

Fecha: 17 de marzo de 2026 **Firma:**

Abstract

Understanding how dark matter (DM) halos acquire and evolve their angular momentum is essential to unravel the connection between halo properties and the surrounding cosmic web. In the linear regime, Tidal Torque Theory (TTT) predicts that proto-halos gain their spin through tidal interactions. However, deviations from these predictions emerge once nonlinear processes, mergers, and environmental effects become dominant. In this work, we study the evolution of the spin alignments of DM halos with respect to the filaments of the cosmic web, focusing on the physical mechanisms that shape their orientation over time. In particular, we explore how halo mass, proximity to filaments, and major mergers influence the persistence or loss of alignment.

We perform a suite of dark matter-only zoom-in N-body simulations centered on ten filaments extracted from a cosmological box using the 1DREAM structure finder. The zoom-in technique allows us to resolve low-mass dark matter halos within each filament while preserving the large-scale environment. Halos are identified with Amiga Halo Finder (AHF), and their evolutionary histories are reconstructed to track the spin, shape, and distance to the filament from redshift $z = 1$ to $z = 0$.

We confirm a strong mass-dependent alignment signal: low-mass halos tend to align parallel to the filament axis, while high-mass halos preferentially exhibit a perpendicular orientation. Predominantly perpendicular alignments begin to dominate toward halo masses of order $\log_{10}(M_h/h^{-1}\mathrm{M}_{\odot}) \sim 12$, corresponding to the most massive bins in our sample. Our analysis shows that this behavior is primarily driven by halo mass and remains robust against variations in the local filament density. We identify major mergers as one of the mechanisms capable of inducing sharp spin reorientations and driving temporary transitions toward prolate shapes. The impact of these mergers is most pronounced for massive halos located near the filament core, suggesting the presence of a preferential merger direction within the filament.

Overall, our results indicate that halo mass is the primary factor governing spin–filament alignments in our sample. Major mergers, although relatively rare, are capable of producing strong and coherent deviations from the pre-existing alignment, particularly for massive halos. In contrast, halos evolving through smoother assembly histories tend to preserve an alignment signal that appears largely established by redshift $z \sim 1$ and subsequently evolves only gradually. This suggests that the commonly reported mass-dependent transition in alignment should be interpreted as a progressive trend rather than the outcome of a single dominant mechanism.

Acknowledgment

First and foremost, I would like to thank my entire family for their unconditional support throughout my academic journey. I express my sincere gratitude to Dr. Antonio Montero-Dorta, my supervisor, for his guidance and constant support throughout this research process. I also want to thank my co-advisor Dr. Rory Smith, because without his help, this work would not have been possible.

I also want to thank my closest friends, who have been constant companions and a source of strength during my time at the university. I appreciate the collaboration of Dr. Katarina Kraljic and Dr. Pablo López, for giving me great opportunities to discuss the results and for all the feedback they gave me.

Contents

Chapter 1

Introduction

The current paradigm of cosmic structure formation establishes that the Large-Scale Structure (LSS) of the Universe arises from small primordial fluctuations in the density field, generated in the early Universe and amplified by gravitational instability. In the linear regime, these perturbations grow proportionally to the cosmic expansion factor while preserving their initial phases, a process accurately described by linear theory and the Zel'dovich approximation (Zel'dovich, 1970).

As the density contrast increases and the evolution becomes non-linear, gravitational collapse proceeds in an intrinsically anisotropic manner, governed by the large-scale tidal field. Matter collapses first along the direction of maximum compression, leading to the formation of sheet-like structures, followed by filamentary structures and, finally, dense nodes at their intersections (Zel'dovich, 1970; Bond et al., 1996). This sequence of anisotropic collapse gives rise to the Cosmic Web, a complex network that dominates the matter distribution on megaparsec scales and encodes the geometry of the underlying tidal field.

Within this framework, the Cosmic Web provides a natural description of the hierarchical and multiscale organization of matter into voids, walls, filaments, and nodes, each associated with distinct dynamical regimes and accretion patterns. Matter flows coherently from underdense regions toward higher-density environments, being funneled along filaments into nodes, where mass assembly is most efficient (Bond et al., 1996). These coherent flows not only regulate the growth of structures but also imprint preferred directions that influence the acquisition of angular momentum and the internal properties of collapsing systems.

As a result, dark matter halos form and evolve embedded within this anisotropic large-scale environment, growing hierarchically through mergers and continuous accretion from the surrounding Cosmic Web (Press and Schechter, 1974; Peebles, 1980). Once virialized, these halos constitute the fundamental building blocks of galaxies and galaxy clusters. Their assembly histories and structural properties are therefore intimately linked to the geometry and dynamics of the large-scale tidal field in which they reside, motivating detailed studies of the connection between halo evolution and the Cosmic Web.

1.1 Tidal Torque Theory

According to the Tidal Torque Theory (TTT), the angular momentum of proto-halos is generated during the early stages of structure formation by tidal torques exerted by the surrounding mass distribution, arising from the misalignment between the inertia tensor and the local tidal field (Hoyle, 1951; Peebles, 1969; Doroshkevich, 1970; White, 1984). These tidal shears, produced by asymmetries in the gravitational potential, induce coherent torques that efficiently build up angular momentum in the linear regime. However, tidal torques become progressively inefficient once a proto-halo decouples from the cosmic expansion and undergoes collapse. After this stage, the proto-halo separates from neighboring perturbations while its moment of inertia decreases rapidly, effectively freezing the angular momentum acquired during the TTT phase (Porciani et al., 2002a,b).

1.2 Halo Alignments

The spin alignments of DM halos have been widely studied with respect to its surrounding LSS, using cosmological N-body simulations. Initially, early studies were contradictory regarding the distribution and behavior of spin alignments. While several studies using N-body simulations have investigated the orientation of halo spins relative to filaments, Hahn et al. (2007); Sousbie et al. (2009); Zhang et al. (2009) reported that halo spins tend to be preferentially perpendicular to the filament direction, independent of halo mass. In contrast, Faltenbacher et al. (2002) found that the spin orientation is distributed randomly in the plane perpendicular to the filaments, while Hatton and Ninin (2001) suggested a tendency for halo spins to align along the filament.

Currently, there is general agreement that the spin orientation of DM halos and galaxies is not random; rather, it is correlated with the large-scale structure in which they reside, as well as with their mass. In particular, this work focuses on filaments of the cosmic web. More recent work has shown that the orientation of the halo spin vector is mass-dependent (e.g., Codis et al., 2015; Ganeshaiah Veena et al., 2018; Codis et al., 2018; Kraljic et al., 2020; Ganeshaiah Veena et al., 2021). This mass-dependent alignment behavior, often related to a phenomenon known as spin-flip, suggests a transition in the angular momentum acquisition process depending on halo mass and environment (Codis et al., 2012; Pichon et al., 2014), leading to the so-called transition mass, where the alignment behavior of halos changes. Theoretically, this inversion has been commonly interpreted by different studies as a consequence of the interplay between large-scale tidal flows and local accretion geometry. In this framework, vorticity is described as being generated in the multi-stream regions of the cosmic web (Libeskind et al., 2013; Laigle et al., 2015). Low-mass halos, which form earlier, are embedded within these flows and, according to this scenario, tend to acquire spin parallel to the filament axis due to the winding of flows around the filament (Codis et al., 2012). Conversely, more massive halos, which form later, are thought to grow primarily through mergers and diffuse accretion flowing along the filament spine. This directional accretion is expected to generate angular momentum perpendicular to the filament axis, leading to the observed mass-dependent transition (e.g., Bett and Frenk, 2012; Welker et al., 2014; Laigle et al., 2015; Ganeshaiah Veena et al., 2018; Krolewski et al., 2019; Ganeshaiah Veena et al., 2021).

The transition mass is a widely studied topic, particularly regarding its dependence on redshift and simulation parameters such as box size. In early studies, limitations in the dynamic mass range led to seemingly contradictory results, suggesting in some cases that no transition existed. For instance, Hatton and Ninin (2001) analyzed halos with masses below 10^{12} M$_\odot$ in a 100 h^{-1}Mpc box and found spin alignments strictly parallel to the filament. Conversely, Faltenbacher et al. (2002) studied more massive halos ($> 10^{14}$ M$_\odot$) in a larger 500 h^{-1}Mpc box and observed a perpendicular trend. Current consensus establishes that these findings essentially probed different ends of the same mass-dependent transition (Codis et al., 2012; Pichon et al., 2014).

Moreover, it has been demonstrated that the transition mass is not universal but depends on the environmental scale, such as filament thickness and density. Aragon-Calvo and Yang (2014) demonstrated that the transition mass varies with the hierarchical level of the filament. Similarly, Ganeshaiah Veena et al. (2018, 2021) showed that the transition mass increases with filament diameter, a behavior linked to the accretion dynamics described by Borzyszkowski (2018). In this context, our work benefits from analyzing a controlled sample of filament with similar scales, allowing us to isolate the mass dependence.

For shape alignments, the interpretation is relatively straightforward, as they are largely imprinted by the initial physical processes governing the ellipsoidal collapse during structure formation (e.g., Forero-Romero et al., 2014). These processes naturally induce a preferred orientation of halos with respect to the surrounding large-scale tidal field, leading to a coherent alignment pattern that reflects the anisotropic nature of gravitational collapse. In particular, the minor axis of halos tends to be preferentially perpendicular to the filament, while the major axis is aligned parallel to it (Lee and Pen, 2001; Aragón-Calvo et al., 2007; Hahn et al., 2007; Shao et al., 2016; Ganeshaiah Veena et al., 2018; López et al., 2021). An analogous effect is also observed for galaxies (Codis et al., 2018). This is a consequence of the sequential nature of collapse: first, a one-dimensional collapse forms sheets, then a two-dimensional collapse forms filaments, and finally, a three-dimensional collapse occurs as matter flows along filaments into nodes (e.g., Zel'dovich, 1970; Codis et al., 2015).

A closely related framework to these alignment studies is that of intrinsic alignments (IA), which describe coherent correlations between the orientations of galaxies and dark matter halos induced by large-scale tidal fields (Hirata and Seljak, 2004; Troxel and Ishak, 2015). Intrinsic alignments provide a valuable probe of structure formation, but also represent a major astrophysical systematic in weak-lensing and large-scale-structure analyses (Hikage et al., 2019; Fabbian et al., 2019, see Chisari 2025 for a comprehensive review). Numerical and hydrodynamical simulations have shown that halo and galaxy spins and shapes exhibit mass- and environment-dependent alignments with the local tidal field (Chisari et al., 2015). In this context, understanding how halo spin–filament alignments evolve, and how they are affected by non-linear processes such as mergers and anisotropic accretion, is essential for connecting IA models to the underlying assembly history of halos.

Observationally, these alignments have also been confirmed for galaxies, where not only mass is a determinant factor, but also morphology plays a key role in the resultant orientation of the spin with the surrounding structure, most outstandingly so in the finding by Tempel et al. (2012) that massive elliptical galaxies tend to have their spin perpendicular to their host filaments while the spin of less massive bright spirals has a tendency to lie parallel to their host filaments (Jones et al., 2010; Tempel and Libeskind, 2013; Zhang et al., 2013, 2014; Hirv, A. et al., 2017; Kraljic et al., 2020). More recent work by Kraljic et al. (2021) further confirmed this morphological dependence using data from the MaNGA survey showing that the alignment is also critically dependent on the galaxy's kinematics (specifically, the degree of ordered stellar rotation). Their findings indicate that spiral galaxies (Late-type) tend to align parallel to the filaments, a signal dominated by low-mass systems. Conversely, S0-type galaxies (elliptical-like) maintain a perpendicular orientation, often linked to lower kinematic support or misalignment between stellar and gas components. This highlights the importance of morphological and kinematic selection in detecting a statistically significant alignment signal.

1.3 Aims and Motivation

Recent work by Storck et al. (2024) adopted a novel experimental approach using the 'splicing' technique to strictly isolate the effect of the cosmic web on halo properties. By simulating specific Milky Way-mass halos at varying distances from a filament while fixing their initial density and tidal fields, they demonstrated that spin orientation is highly sensitive to non-linear coupling with the environment, showing fluctuations of up to 80%.

Similar to this controlled experimental setup, our work investigates the natural dynamical evolution of a broad population of halos within their host filamentary environments. To capture the key drivers of spin alignment—specifically the wide range of halo masses and the stochastic nature of merger histories—within a self-consistent cosmological context, we adopted a targeted numerical strategy. Rather than relying on large-volume simulations, which often lack the resolution required for detailed halo identification, we generated a suite of DM-only N-body simulations tailored specifically to this study. We employ the zoom-in technique, which offers the advantage of achieving high dark-matter particle resolution in filamentary regions without requiring excessive computational resources. This enables us to resolve a wide range of halo masses from $10^{9.5}\ h^{-1}\mathrm{M}_\odot$ to $10^{13.5}\ h^{-1}\mathrm{M}_\odot$, providing high confidence in the low-mass regime, where these halos constitute the dominant population in our sample. All of this is performed while preserving the surrounding large-scale cosmological environment.

The main goal of this paper is to investigate the different drivers of spin alignment and to disentangle whether the signal observed at redshift z=0 reflects an intrinsic evolutionary trend of halo spin alignments, or whether it is instead the outcome of external mechanisms — such as the influence of the local filamentary environment or highly disruptive events like major mergers. Although this study focuses exclusively on DM halos, these structures define the gravitational potential wells in which galaxies reside. While baryonic physics—such as gas cooling, feedback, and star formation—can induce misalignments between the galaxy spin and the halo spin (Tenneti et al., 2014; Velliscig et al., 2015; Jiang et al., 2019), the alignment trends established by the DM halo impose a foundational constraint on the galaxy's orientation relative to the cosmic web. By isolating the DM dynamics, we aim to understand the purely gravitational baseline upon which baryonic processes subsequently act. In particular, we explore how major mergers influence halo orientations, and whether certain halos maintain their alignment over time while others undergo significant reorientation. We examine the spatial distribution of halos that preserve or lose their alignment, and investigate if proximity to filaments tends to enhance alignment. Since the halos studied in this work are, by construction, collapsed systems, our analysis probes a post-TTT evolutionary stage, in which nonlinear processes such as mergers, anisotropic accretion, and environmental interactions dominate the subsequent evolution of halo spin and shape. In particular, within the filamentary environment of the cosmic web, these processes are expected to imprint correlations between halo angular momentum, halo shape, and the large-scale structures in which they are embedded (Aragón-Calvo et al., 2007).

This thesis is organized as follows. Chapter 2 describes the numerical setup, including the simulations, halo identification, and filament reconstruction. Chapter 3 presents the alignment results and their evolution with redshift, as well as the analysis of the main drivers of spin reorientation. Chapter 4 discusses the physical interpretation of these results. Finally, Chapters 5 and 6 summarize the conclusions and outline possible future work.

Chapter 2

Methods

This chapter details the numerical tools and methodology employed to model the non-linear evolution of dark matter halos within the cosmic web. We begin by describing the algorithms used for generating cosmological initial conditions and for evolving the N-body dynamics. Finally, we describe the specific parameters and ”zoom-in” configuration of the simulation suite performed for this work.

2.1 MUSIC

The MUlti-Scale Initial Conditions code (MUSIC; Hahn and Abel, 2011) is used to generate the cosmological initial conditions for the zoom-in simulations. MUSIC allows the construction of multi-resolution initial conditions, enabling high-resolution regions to be embedded within a lower-resolution cosmological volume while preserving consistency with the input linear matter power spectrum.

The code generates particle displacements and velocities using Lagrangian Perturbation Theory (LPT). In this work, second-order LPT (2LPT) is employed to improve the accuracy of the initial density and velocity fields at early times. The multi-resolution capability of MUSIC ensures that the refinement region remains consistent with the large-scale modes of the simulation box, which is essential for properly modeling the formation of structures within the selected filaments.

2.2 RAMSES

RAMSES (Teyssier, 2002) is an adaptive mesh refinement (AMR) N-body code designed to study structure formation in a cosmological context. The code relies on the Adaptive Mesh Refinement technique to increase spatial resolution in high-density regions. Its fundamental data structure is the Fully Threaded Tree (FTT), which allows recursive cell-by-cell refinements organized into groups of eight cells (“octs”). Each oct contains pointers to its parent, neighbors, and children, enabling efficient navigation across refinement levels. Refinement follows a quasi-Lagrangian criterion, where cells are refined once the particle number exceeds a given threshold, maintaining an approximately constant number of particles per cell.

The dark matter component is treated as a collisionless system governed by the Vlasov–Poisson equations. Gravitational forces are computed using a Particle–Mesh (PM) method. The Poisson equation is solved with a multigrid relaxation scheme on refined levels, while Fast Fourier Transforms (FFT) are used on the coarse base grid. This approach allows an accurate computation of gravity across different refinement levels.

Time integration is adaptive, with smaller time steps assigned to higher refinement levels according to local stability conditions. The integration scheme is second-order accurate and reduces to a standard leapfrog scheme when constant time steps are used.

2.3 N-body simulation

We performed an initial cosmological N-body simulation consisting of 128^3 equal-mass DM particles within a cubic box of side length 100 h^{-1}Mpc (hereafter referred to as the level-7 simulation, since it considers $2^7 = 128$ particles in each side of the box). Each DM particle has a mass of $m_{\mathrm{DM}} \approx 5.21 \times 10^{10}\ h^{-1}\mathrm{M}_{\odot}$. The initial conditions were generated using the MUSIC code (Hahn and Abel, 2011) previously described, adopting the standard ΛCDM cosmological model with parameters $\Omega_m = 0.315$, $\Omega_b = 0.049$, $\Omega_\Lambda = 0.685$, $H_0 = 67.4$ km s^{-1} Mpc^{-1}, and $\sigma_8 = 0.811$, consistent with the Planck 2018 base-ΛCDM results (Planck Collaboration et al., 2020), initialized at redshift $z = 40$. The simulations were evolved down to $z = 0$ using the publicly available AMR code RAMSES (Teyssier, 2002).

2.4 1Dream

To identify filamentary structures in the simulation volume, we applied the 1DREAM framework (Canducci et al., 2022) to the $z = 0$ snapshot of the level-7 simulation. 1DREAM is a novel machine-learning toolbox designed to robustly recover low-dimensional manifolds (such as filaments) in noisy environments (e.g., Awad et al., 2023; Raj et al., 2024). The structure extraction pipeline consists of four sequential steps:

- LAAT (Locally Aligned Ant Technique): A swarm-intelligence algorithm that uses simulated pheromones to highlight high-density regions and remove background noise particles that do not belong to any structure.
- MBMS (Manifold Blurring Mean Shift): A denoising algorithm that iteratively moves the remaining particles toward the local density ridge, effectively collapsing the structure onto its central axis.
- DimIndex (Dimensionality Index): A classifier that computes the local dimensionality of the manifold, allowing us to distinguish between clusters and filaments.
- Crawling: A graph-based algorithm that traces the connected 1D skeleton (spine) of the filament by linking the density peaks identified in the previous steps.

2.5 Zoom-in simulations

In this initial step, we employed only the LAAT module to remove noisy particles and enhance the contrast of large-scale structures. From the resulting filament network, we selected a sample of ten filaments through visual inspection, requiring that (i) their curvature to be negligible, (ii) their lengths be comparable, and (iii) both ends of each filament be connected to group-mass halos with $12.8 \leq \log_{10}(M_h/h^{-1}\mathrm{M}_\odot) \leq 13.7$, which were confirmed during the halo selection process described in Section 2.7. The selected filament sample is listed in Table 2.1, where we report some of its main properties, such as the filament length, the number of DM particles enclosed within each filament in the level-7 simulation, and its particle number density, computed within cylindrical volumes of radius 3 h^{-1}Mpc around the filament spine. As can be seen, the selected filaments have similar properties.

Table 2.1: Properties of the selected filaments at redshift $z = 0$ in the level-7 simulation, including the filament length (in h^{-1}Mpc), the number of particles associated with each filament, and the particle density computed assuming a cylindrical volume with radius $3\,h^{-1}$Mpc.

Filament	Length h^{-1}Mpc	DM particles	Density $\#/h^{-3}$Mpc^3
1	15.33	801	1.85
2	9.25	1844	7.05
3	8.15	1325	5.75
4	9.20	723	2.78
5	10.98	864	2.78
6	9.53	961	3.57
7	8.29	575	2.45
8	7.63	535	2.48
9	12.16	869	2.53
10	11.05	751	2.40

To implement the zoom-in procedure, we use the particles associated with the filaments previously identified in the uniform-resolution (unigrid) level-7 simulation. For every filament, we trace the corresponding particles back to the initial conditions and define an ellipsoidal Lagrangian region that is sufficiently large to enclose all particles that will eventually end up in the filament at the final snapshot. This ellipsoidal region is adopted as the high-resolution target volume for that filament, and a new set of multi-scale initial conditions is generated, in which the resolution is increased inside the zoom region — reaching a maximum refinement level of 11 (corresponding to a minimum dark matter particle mass of $m_{\mathrm{DM}} \simeq 1.01 \times 10^7\ h^{-1}\mathrm{M}_\odot$) while the surrounding environment remains at lower resolution. Each of these initial-condition sets is then used to run an independent zoom-in simulation.

The zoomed-in regions of the ten filaments are shown in Fig. 2.1 (highlighted in blue), illustrating that the structures identified in the level-7 simulation remain unchanged at large scales, while the mass resolution within the refined regions is significantly enhanced.

The primary analysis was performed on the $z = 0$ snapshot, while for the evolutionary study we considered several intermediate redshifts spanning the range $0 \leq z \leq 1$, to ensure that the effects analyzed are fully within the nonlinear regime. Throughout this work, all the analysis is restricted to the highest-resolution (level-11) regions of the zoom-in simulations. This approach allows us to robustly resolve low-mass halos within filaments while maintaining a self-consistent cosmological environment.

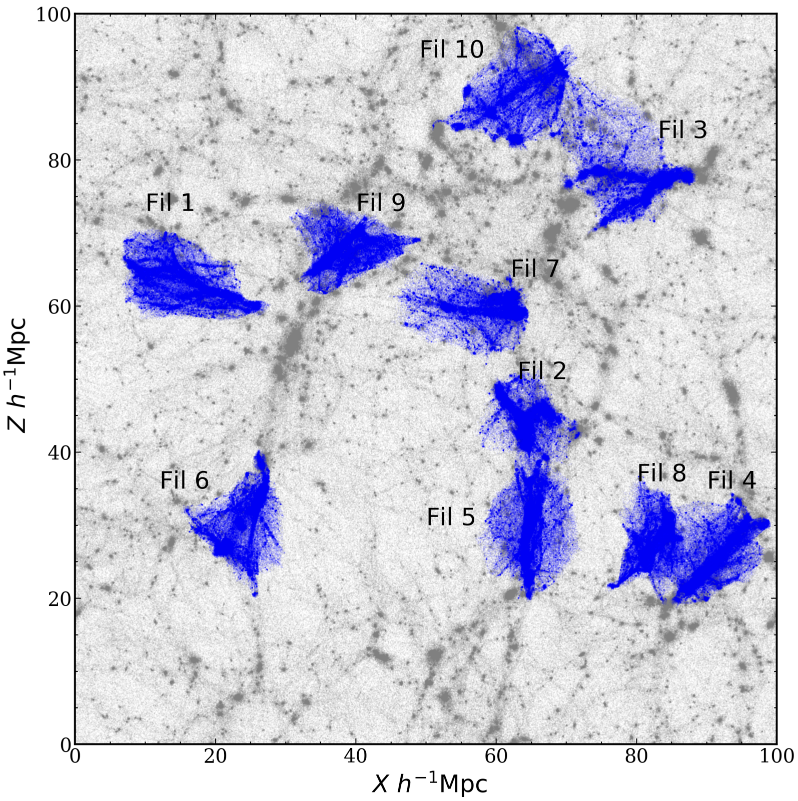

Figure 2.1: Side view of the zoomed-in region corresponding to the ten filaments at redshift 0 colored in blue. Gray represents the particles of the level-7 initial simulation.

2.6 Filament across redshift

To quantify the local environment of the dark matter halos, we computed the perpendicular distance from each halo to the filament's central axis (or spine) as a function of redshift. This analysis utilizes again the previously mentioned set of tools 1DREAM, now employing a sequence of its core modules—LAAT, MBMS, DimIndex, and Crawling—to robustly extract the filamentary skeleton.

In order to reconstruct our filament distances, one possible approach would be to identify and track the filament independently at each snapshot of interest. However, this strategy would increase the computational cost and introduce additional uncertainties, since noise can accumulate differently at each redshift and lead to inconsistencies in the filament reconstruction. Instead, we identified filaments at the highest redshift considered in our analysis, which allows us to trace the densest and dynamically dominant regions of the structure and ensures a coherent definition of the filament backbone. Our reconstruction strategy follows a retrograde–anterograde tracking scheme. We define the filament geometry at redshift $z = 1$, where the structure is already well established but is still less affected by the strong non-linear shell-crossing in the core. The procedure consists of four steps: (i) LAAT is used to remove background noise; (ii) MBMS collapses the remaining particles toward the local density ridge; (iii) DimIndex identifies and removes the densest regions (nodes); and (iv) the Crawling algorithm traces the connected filamentary structure between these nodes, obtaining the particle distribution that defines the filament.

This combination yields a continuous and topologically robust definition of the filament spine

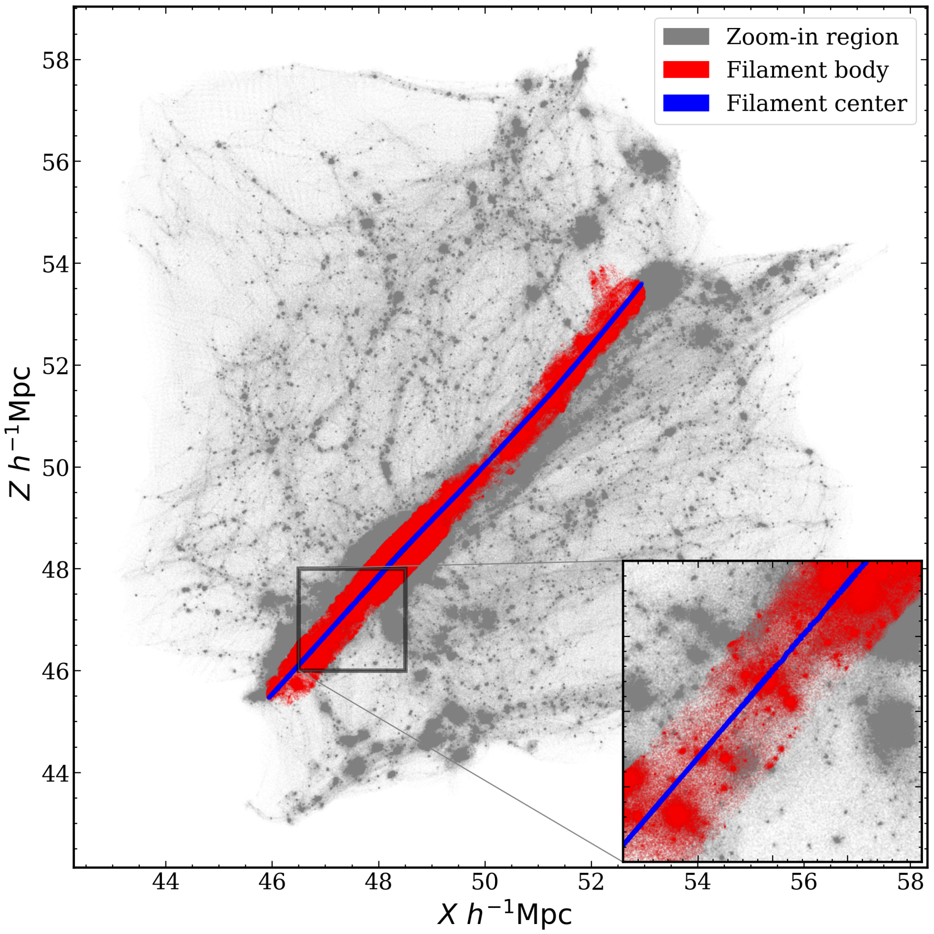

Figure 2.2: Side view of the zoomed-in region corresponding to filament 4 at redshift 1. Gray represents the particles of the level-11 zoom-in region, red shows the filament body detected by Crawling, and blue indicates the particles collapsed to the filament center by MBMS.

at $z = 1$. We then tracked the particles belonging to this spine across all snapshots down to $z = 0$, re-applying MBMS at each step to follow the evolution of the filament's physical "backbone".

For each halo identified in Section 2.7, we defined its distance d to the filament as the minimum Euclidean distance between the halo's center of mass and the reconstructed filament spine at the corresponding redshift. This provides a consistent, time-resolved metric of the halo's proximity to the deep potential well of the filament.

Figure 2.2 illustrates the different regions identified for Filament 4 at $z = 1$. The gray points represent the full dark matter particle distribution in the high-resolution region, the blue points indicate the particles collapsed by MBMS, and the red line shows the final filament body detected by Crawling.

2.7 Halo properties

For halo identification, we use the AMIGA Halo Finder (hereafter AHF) code (Knollmann and Knebe, 2009), which identifies gravitationally bound structures in N-body simulations using the

Friends-of-Friends (FOF) method (Huchra and Geller, 1982). Due to the high resolution achieved by the zoom-in simulations, AHF is able to resolve a large number of low-mass DM halos. We impose a minimum of 100 particles per halo, which allows us to resolve halos down to a minimum mass of $10^9\ h^{-1}\mathrm{M}_\odot$. For this work, however, we adopt a more conservative lower mass limit $10^{9.5}\ h^{-1}\mathrm{M}_\odot$, corresponding to a minimum of 311 DM particles per halo. This choice helps to avoid resolution artifacts. As expected, more massive halos are less abundant. This trend is illustrated in Fig. 2.3, which shows the mass distribution of halos associated with the ten filaments. The imposed mass cut is indicated by the red dashed line.

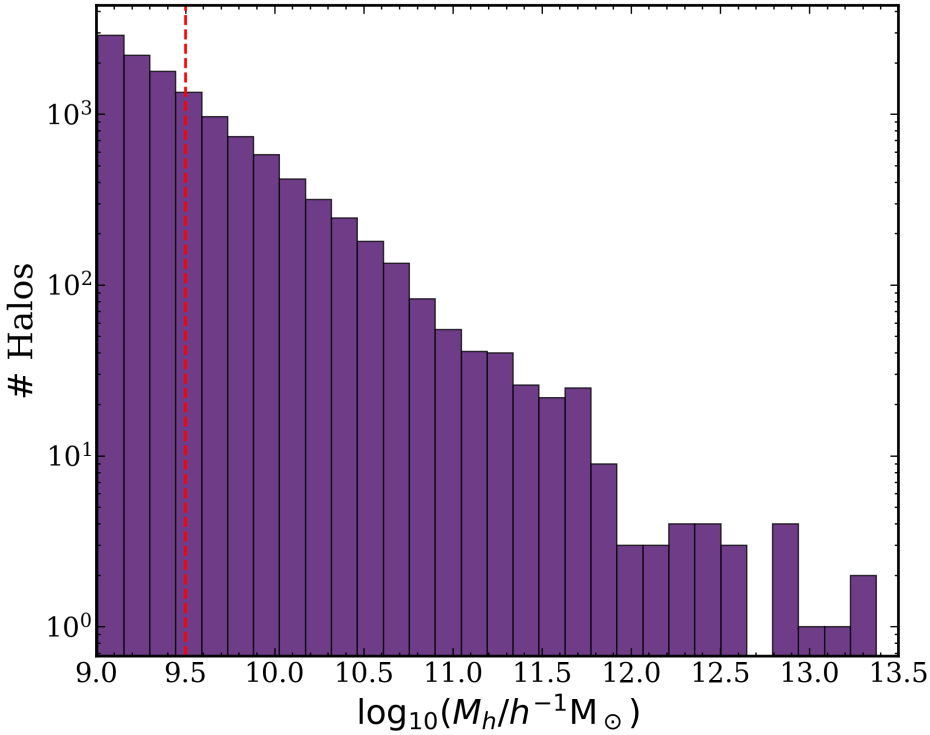

Figure 2.3: Mass distribution of halos associated with the ten selected filaments. The red dashed line indicates the mass cut applied in our analysis.

Halo DM particles may not be strongly bound, but the angular momentum from each individual particle contributes to the total halo spin, defined as the sum over the angular momentum of all the DM particles that compose the halo:

$$\mathbf{J} = \sum_{n=1}^{N} m_n(\mathbf{r}_n \times \mathbf{v}_n), \tag{2.1}$$

where $\mathbf{r}_n$ and $\mathbf{v}_n$ denote the position and velocity of the n-th particle relative to the halo center of mass, and m_n is its mass.

Commonly, one makes use of the magnitude of the angular momentum, $J = |\mathbf{J}|$, to quantify the spin by using the spin parameter λ, first introduced by Peebles (1969). This spin parameter quantifies the level of coherence in the rotation of the halo. A value close to unity indicates that the halo is mainly or purely supported by rotation (Padmanabhan, 1993), while a value closer to zero corresponds to halos that are pressure- or dispersion-supported. In this work, we adopt the terms fast rotators and slow rotators to refer to these rotationally supported and dispersion-supported halos, respectively. In this work, we adopt the spin parameter definition of Bullock et al. (2001), denoted as λ'. Defined within a virialized sphere of radius R enclosing a mass M, and with V the halo circular velocity, the spin parameter is given by:

$$\lambda' = \frac{J}{\sqrt{2}MVR}. \tag{2.2}$$

DM halos are commonly referred to as perfect spherical bodies for simplicity. Here, we aim to extend the study to include their shape, taking into account their triaxiality. N-body simulations, in agreement with theoretical and observational studies, indicate that DM halos deviate from spherical symmetry; numerous studies have found that halos are better represented by ellipsoids (e.g., Jing and Suto, 2002; Bailin and Steinmetz, 2005; Kasun and Evrard, 2005; Allgood et al., 2006; Hayashi et al., 2007; Vera-Ciro et al., 2011; Bonamigo et al., 2015; Butsky et al., 2016; Prada et al., 2019). To determine the shape of the halo, we make use of its reduced moment of inertia tensor, $\tilde{I}_{ij}$. The reduced inertia tensor is a 3×3 symmetric matrix, defined as

$$\tilde{I}_{ij} = \sum_{k=1}^{N} \frac{m_k r_{k,i} r_{k,j}}{r_k^2}, \tag{2.3}$$

where r_k is the distance of the k-th particle from the halo center. This tensor can be diagonalized to calculate its eigenvalues, $s_a \geq s_b \geq s_c$, and eigenvectors $\vec{E}_a$, $\vec{E}_b$ and $\vec{E}_c$, which denote the major, intermediate, and minor axes of the halo respectively. We describe the shape of the halos using the triaxiality parameter T, defined as

$$T = \frac{1 - q^2}{1 - s^2}, \tag{2.4}$$

in terms of the axis ratios $q = b/a$ and $s = c/a$, where $a = \sqrt{s_a}$, $b = \sqrt{s_b}$, and $c = \sqrt{s_c}$. This parameter allows us to classify the shape of halos into three regimes: when $T \to 0$, halos tend to be oblate, that is, two dominant axes ($a \simeq b \gg c$); for intermediate values of T, halos are triaxial, meaning none of the axes dominates significantly; and when $T \to 1$, halos are prolate, with a single dominant axis ($a \gg b, c$).

In addition to halo mass, AHF provides a wide range of phys- ical properties, including velocity, inertia tensor components, halo radius, and angular momentum components, among others. Using the latter, we extract the spin vector of each halo in the zoomed-in region, as previously defined, in order to study its alignment with the corresponding filament direction.

Regarding the evolution of the filament body, we also track the evolution of halos using AHF. In addition to the main halo-finding tool, we use two complementary utilities: MergerTree, which provides information about the merger history of halos across different snapshots; and ahfHaloHistory, which links the MergerTree output and produces individual files describing the evolution of each halo, reporting the properties of the most massive progenitor of each halo.

Chapter 3

Results

In this chapter we present the alignment results obtained from the ten zoom-in filaments. We begin by characterizing the spin–filament alignment at redshift $z = 0$, separating halos by mass and distance to the filament. We then extend the analysis to $0 \leq z \leq 1$ to study how this signal evolves over time. Finally, we examine the main mechanisms associated with spin reorientation, focusing on different drivers of spin alignments.

3.1 Spin and shape alignments at z=0

In this section, we focus on the alignment of halos with respect to their host filaments at $z = 0$, where we adopt the mass cut previously mentioned in Section 2.7 and, in addition, consider only central halos that are enclosed within a cylindrical region of radius 3 h^{-1}Mpc around the filament axis. This selection results in a total of 5,297 DM halos.

To quantify the alignments, we compute the angle θ between two vectors, $\mathbf{v}_1$ and $\mathbf{v}_2$. Since no preferred direction is assumed for the filament, we adopt the standard convention of restricting θ to the range $[0, \pi/2]$ (e.g., Aragon-Calvo and Yang, 2014; Ganeshaiah Veena et al., 2018). This is operationally defined by the absolute value of the dot product:

$$\cos\theta = \frac{|\mathbf{v}_1 \cdot \mathbf{v}_2|}{|\mathbf{v}_1||\mathbf{v}_2|}. \tag{3.1}$$

In this work, we apply this definition to measure the alignment between: (i) the halo spin and the filament axis ($\mathbf{v}_1 = \mathbf{J}, \mathbf{v}_2 = \mathbf{e}_{\text{fil}}$), (ii) the halo shape principal axes and the filament ($\mathbf{v}_1 = \mathbf{E}_{a,b,c}, \mathbf{v}_2 = \mathbf{e}_{\text{fil}}$), and (iii) the internal alignment between the halo spin and its shape ($\mathbf{v}_1 = \mathbf{J}, \mathbf{v}_2 = \mathbf{E}_{a,b,c}$).

Figure 3.1 illustrates an arbitrary distribution of DM halos along a filament, highlighting three halos denoted as H_1, H_2, and H_3, which represent different types of alignment with the filament vector, shown as a blue arrow. The angle between the filament and the spin vector of each halo is also indicated. H_1 is aligned parallel to the filament, with an angle of 0 between its spin vector and the filament direction, yielding an alignment value of 1 since $\cos(0) = 1$. H_3 is oriented perpendicular to the filament, corresponding to an angle of $\theta = \pi/2$ and an alignment value of 0. Finally, H_2 exhibits an intermediate alignment (or no preferred orientation), resulting in a value close to 0.5.

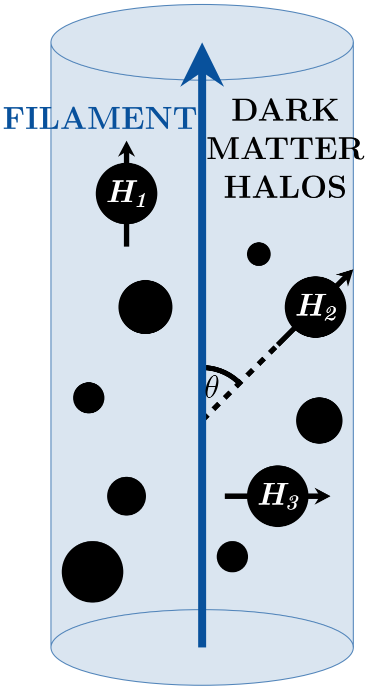

Figure 3.1: Sketch of the problem involving three halos, labeled H_1, H_2, and H_3 in black, including their spin directions, next to a filament whose direction is represented by a blue arrow and whose shaded area indicates its total extent. We can see that the three halos have different orientations, which can be related by the angle θ shown in the figure.

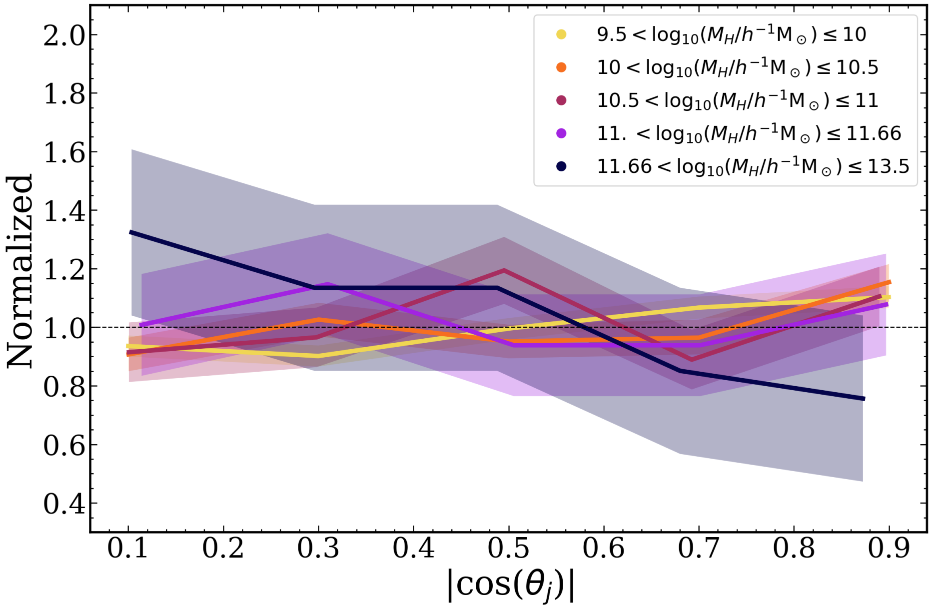

Figure 3.2: Stack of the spin-filament alignment distributions for the sample of 10 filaments. The panel shows histograms normalized to unity, separated into different mass bins as indicated by the legend. The shaded regions represent the 1σ uncertainty estimated via bootstrap resampling.

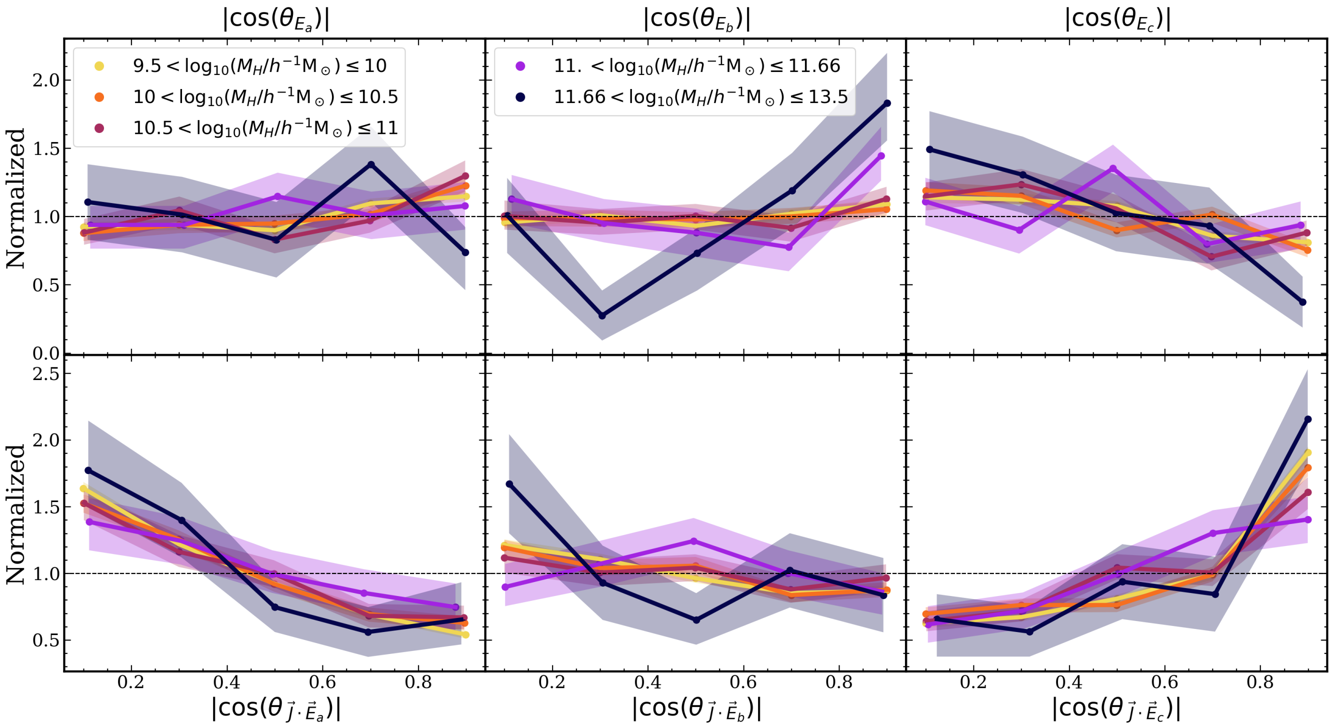

Figure 3.3: Similar as in Figure 3.2, but for the alignments related to the components of the inertia tensor. The top three panels show the alignment between the major axis, the second major axis and the minor axis, denoted by $\mathbf{E}_a, \mathbf{E}_b, \mathbf{E}_c$ respectively, and the filament direction. In each panel, halos are separated into different mass bins. The bottom three panels display the dot product between the spin vector $\mathbf{J}$ and each of the inertia tensor axes, using the same mass binning as in the top panels. Again the shaded regions represent the 1σ uncertainty estimated via bootstrap resampling.

With this in mind, we stack all the alignment values of halos from the 10 filaments that make up our sample. To properly interpret the behavior, it is crucial to separate the sample by halo mass. The distribution of $|\cos\theta_j|$ for all halos located within our sample filaments at redshift 0 is shown in Figure 3.2 in different halo mass bins, where the number of halos in each mass bin is normalized so that the area under the curve equals 1. This mass-based division is motivated by the discussion in Section 1, where it was established that halo mass plays a significant role in the alignment with respect to the host filament.

To assess the statistical significance of the alignment signals, we estimate the uncertainties using a bootstrap resampling technique. These are shown as shaded regions in Figures 3.2 and 3.3. As observed in the plots, the uncertainty intervals widen for the highest mass bin. This behavior is expected and reflects the hierarchical nature of structure formation, where the abundance of halos decreases rapidly with increasing mass. Consequently, the highest mass bin contains a smaller sample size compared to the low-mass population, leading to larger statistical fluctuations, as also noted in similar studies (e.g., Ganeshaiah Veena et al., 2018). To complement the bootstrap estimation and robustly quantify the deviation from a random orientation, we performed a Kolmogorov-Smirnov (KS) test against a uniform distribution (Table 3.1). The test confirms a highly significant alignment signal for the lowest mass regime ($p \sim 10^{-5}$), while intermediate

Table 3.1: Kolmogorov-Smirnov (KS) test results for the halo spin alignment. The table presents the KS statistic D and the corresponding p-value for different halo mass ranges, evaluating the null hypothesis of a uniform random distribution.

Mass Range $\log_{10}(M_H/h^{-1}\mathrm{M}_\odot)$	Statistic D	p-value
$9.5 < M \leq 10.0$	0.0414	8.46×10^{-5}
$10.0 < M \leq 10.5$	0.0336	1.51×10^{-1}
$10.5 < M \leq 11.0$	0.0333	7.54×10^{-1}
$11.0 < M \leq 11.7$	0.0432	9.36×10^{-1}
$11.7 < M \leq 13.5$	0.1335	2.57×10^{-1}

masses are statistically consistent with random orientations. Notably, the KS statistic D reaches its maximum value ($D \approx 0.13$) in the highest mass bin; however, the corresponding p-value ($p \approx 0.26$) indicates this deviation is not statistically significant. This behavior is a direct consequence of the aforementioned low number statistics at the massive end, which prevents the test from completely ruling out random fluctuations. Nevertheless, the transition from a parallel tendency at low masses to a perpendicular one at high masses remains distinguishable despite the increased variance in the massive end.

The results reveal a clear mass dependence in the alignment signal. Low-mass halos exhibit a tendency to align parallel to the filament axis, whereas the most massive halos show a preferential perpendicular orientation. We identify a transition between these two regimes in our sample occurring near $\log_{10}(M_h/h^{-1}\mathrm{M}_\odot) \sim 12$, where perpendicular alignments begin to dominate the overall trend. In this range, the alignment signal begins to favor a perpendicular orientation, yet the strength of this signal remains weaker than that observed for the highest mass bin. This transition mass is consistent with previous findings (e.g., Codis et al., 2012; Ganeshaiah Veena et al., 2018; López et al., 2019).

So far, our analysis has focused on the orientation of the spin vector relative to the host filament. We now extend this study to the alignment of the halo's shape. Previous studies have established that the minor axes of DM halos tend to be oriented perpendicular to the filaments or walls of the cosmic web (Aragón-Calvo et al., 2007; Hahn et al., 2007; Shao et al., 2016; Ganeshaiah Veena et al., 2018; López et al., 2021), indicating a strong correlation between the halo's geometry and its large-scale environment.

In the top three panels of Figure 3.3, we present the alignment between these three principal axes and the filament vector. Two main results emerge from this analysis. First, unlike the spin vector, the orientation of the inertia tensor components does not exhibit a directional inversion (or 'shape-flip') as a function of halo mass. However, as we will explore in the next section, the *strength* of this alignment does depend on mass. Second, the major and intermediate axes tend to align parallel to the filament, whereas the minor axis is preferentially oriented perpendicular to it (Aragón-Calvo et al., 2007; Hahn et al., 2007; Shao et al., 2016; Ganeshaiah Veena et al., 2018; López et al., 2021). To quantify this, our KS tests against a uniform distribution (Table 3.2) reveal important nuances regarding the statistical robustness of these trends. While the visual tendencies remain consistent, the statistical significance strongly depends on the mass bin and the specific axis. For instance, the parallel alignment of the major axis ($\vec{E}_a$) becomes statistically indistinguishable from a random distribution for masses above $10^{11}h^{-1}\mathrm{M}_\odot$ ($p > 0.6$). Similarly, the intermediate axis ($\vec{E}_b$) shows a weak and often non-significant signal across several bins. In

Table 3.2: Same as Table 3.1, but for the alignment of the halo shape with the filaments ($|\cos(\theta_{E_i})|$) and the internal alignment between the halo's angular momentum and its principal axes ($|\vec{J}\cdot\vec{E}_i|$).

Measurement	Mass Range $\log_{10}(M_H/h^{-1}\mathrm{M}_\odot)$	Statistic D	p-value
$\lvert\cos(\theta_{E_a})\rvert$	$9.5 < M \leq 10.0$	0.0484	2.00×10^{-6}
$\lvert\cos(\theta_{E_b})\rvert$	$9.5 < M \leq 10.0$	0.0306	8.12×10^{-3}
$\lvert\cos(\theta_{E_c})\rvert$	$9.5 < M \leq 10.0$	0.0757	4.52×10^{-15}
$\lvert\cos(\theta_{\vec{J}\cdot\vec{E}_a})\rvert$	$9.5 < M \leq 10.0$	0.1758	8.09×10^{-80}
$\lvert\cos(\theta_{\vec{J}\cdot\vec{E}_b})\rvert$	$9.5 < M \leq 10.0$	0.0645	4.82×10^{-11}
$\lvert\cos(\theta_{\vec{J}\cdot\vec{E}_c})\rvert$	$9.5 < M \leq 10.0$	0.1862	1.43×10^{-89}
$\lvert\cos(\theta_{E_a})\rvert$	$10.0 < M \leq 10.5$	0.0524	3.77×10^{-3}
$\lvert\cos(\theta_{E_b})\rvert$	$10.0 < M \leq 10.5$	0.0166	9.08×10^{-1}
$\lvert\cos(\theta_{E_c})\rvert$	$10.0 < M \leq 10.5$	0.0760	3.78×10^{-6}
$\lvert\cos(\theta_{\vec{J}\cdot\vec{E}_a})\rvert$	$10.0 < M \leq 10.5$	0.1637	4.54×10^{-27}
$\lvert\cos(\theta_{\vec{J}\cdot\vec{E}_b})\rvert$	$10.0 < M \leq 10.5$	0.0608	4.27×10^{-4}
$\lvert\cos(\theta_{\vec{J}\cdot\vec{E}_c})\rvert$	$10.0 < M \leq 10.5$	0.1715	1.07×10^{-29}
$\lvert\cos(\theta_{E_a})\rvert$	$10.5 < M \leq 11.0$	0.0700	3.81×10^{-2}
$\lvert\cos(\theta_{E_b})\rvert$	$10.5 < M \leq 11.0$	0.0323	7.88×10^{-1}
$\lvert\cos(\theta_{E_c})\rvert$	$10.5 < M \leq 11.0$	0.0954	1.31×10^{-3}
$\lvert\cos(\theta_{\vec{J}\cdot\vec{E}_a})\rvert$	$10.5 < M \leq 11.0$	0.1506	2.30×10^{-8}
$\lvert\cos(\theta_{\vec{J}\cdot\vec{E}_b})\rvert$	$10.5 < M \leq 11.0$	0.0493	2.78×10^{-1}
$\lvert\cos(\theta_{\vec{J}\cdot\vec{E}_c})\rvert$	$10.5 < M \leq 11.0$	0.1546	8.63×10^{-9}
$\lvert\cos(\theta_{E_a})\rvert$	$11.0 < M \leq 11.7$	0.0606	6.30×10^{-1}
$\lvert\cos(\theta_{E_b})\rvert$	$11.0 < M \leq 11.7$	0.0785	3.10×10^{-1}
$\lvert\cos(\theta_{E_c})\rvert$	$11.0 < M \leq 11.7$	0.0762	3.43×10^{-1}
$\lvert\cos(\theta_{\vec{J}\cdot\vec{E}_a})\rvert$	$11.0 < M \leq 11.7$	0.1286	1.41×10^{-2}
$\lvert\cos(\theta_{\vec{J}\cdot\vec{E}_b})\rvert$	$11.0 < M \leq 11.7$	0.0911	1.64×10^{-1}
$\lvert\cos(\theta_{\vec{J}\cdot\vec{E}_c})\rvert$	$11.0 < M \leq 11.7$	0.1906	3.76×10^{-5}
$\lvert\cos(\theta_{E_a})\rvert$	$11.7 < M \leq 13.5$	0.0686	9.42×10^{-1}
$\lvert\cos(\theta_{E_b})\rvert$	$11.7 < M \leq 13.5$	0.2293	5.04×10^{-3}
$\lvert\cos(\theta_{E_c})\rvert$	$11.7 < M \leq 13.5$	0.1993	2.16×10^{-2}
$\lvert\cos(\theta_{\vec{J}\cdot\vec{E}_a})\rvert$	$11.7 < M \leq 13.5$	0.2624	7.89×10^{-4}
$\lvert\cos(\theta_{\vec{J}\cdot\vec{E}_b})\rvert$	$11.7 < M \leq 13.5$	0.1709	7.11×10^{-2}
$\lvert\cos(\theta_{\vec{J}\cdot\vec{E}_c})\rvert$	$11.7 < M \leq 13.5$	0.2628	7.69×10^{-4}

contrast, the perpendicular alignment of the minor axis ($\vec{E}_c$) is much more robust, maintaining a clear and significant signal even for the most massive halos ($p \approx 0.02$), which distinguishes it from the global spin-filament alignment that loses significance at the high-mass end.

Additionally, we examine the internal alignment between the spin vector and the halo's shape. The bottom three panels of Figure 3.3 display the angle between the spin vector and each principal axis. We observe a trend inverse to that of the filament alignment: the spin vector tends to be perpendicular to the major and intermediate axes, while showing a strong parallel alignment with the minor axis. Physically, this indicates that these halos—which tend to be prolate—rotate preferentially around their shortest axis. The KS test results further underscore the magnitude of this internal kinematic coupling, though they also highlight its complexity. The deviations from a random distribution are exceptionally highly significant ($p \ll 0.001$) for the major ($\vec{E}_a$) and minor ($\vec{E}_c$) axes across almost the entire mass range, and this correlation persists with high statistical significance even for the most massive halos ($p < 10^{-3}$). However, the alignment with the intermediate axis ($\vec{E}_b$) weakens considerably, losing statistical significance for masses above $10^{10.5} h^{-1}\mathrm{M}_\odot$ ($p > 0.05$). This confirms that while the internal spin-shape relationship exhibits a generally stronger and more resilient signal than the external spin-filament orientation, it is fundamentally dominated by the kinematic coupling with the longest and shortest axes of the ellipsoid.

3.2 Alignment evolution

As mentioned in the Introduction, halos acquire their initial angular momentum through tidal torques during the early linear regime, as described by the TTT. However, several studies (e.g., López et al. 2025) have shown that deviations from TTT predictions already emerge at very high redshift ($z \sim 10$), even before the onset of strong nonlinear evolution. Motivated by this, we focus on the nonlinear regime, where TTT no longer holds, analyzing the spin evolution of our sample of halos down to redshift $z = 1$. Our goal is to gain insight into how nonlinear processes shape the final spin properties observed at $z = 0$. From now on, the sample will change slightly. Previously, we considered main halos located within the cylindrical volume at $z = 0$. We now restrict the sample to halos that can be traced back to $z = 1$, allowing us to follow their spin evolution over the full redshift range. Additionally, we require all selected halos to be centrals at redshift $z = 0$. This yields a sample of 4,797 halos, slightly smaller than that of the previous section, reflecting the effect of the additional constraint.

Figure 3.4 shows the interpolated evolutionary curves of all halos contained in all filaments, grouped by their mass at redshift $z = 0$. The top panel shows the average evolution of the spin alignment. The second and third panels present the average evolution of the alignment of the major and minor components of the inertia tensor, respectively. The fourth panel shows the evolution of the distance between halos and the center of the filament, following the definition provided in Section 2.6. Finally, the bottom panel shows the evolution of the triaxiality parameter T.

From Figure 3.4, we observe—similarly to Figure 3.2—that, when considering the spin alignment with the filament. Halos in the highest $z = 0$ mass bin tend to be more strongly perpendicularly aligned with the filament. Toward lower $z = 0$ masses, the alignment progressively shifts toward a more parallel configuration, although this trend becomes less pronounced in the lowest-mass bin. Another notable result shown in this figure is the remarkable stability of the spin alignment since $z \simeq 1$. Despite halos progressively approaching the filament spine, the alignment signal remains nearly constant over time, as indicated by the almost horizontal evolution of the median curves in the top panels. This indicates that, for the majority of halos, the filament environment does not induce significant reorientation after $z \simeq 1$; instead, the alignment observed at $z = 0$ was already largely established at earlier epochs.

We also track the evolution of the orientation of the inertia tensor's components relative to the filament, focusing primarily on the major and minor axes, shown in the second and third panels, respectively. Similar to the spin alignment, these tracks do not exhibit significant variations with redshift, except for the major axis in the highest mass bin, which exhibits greater variability as it

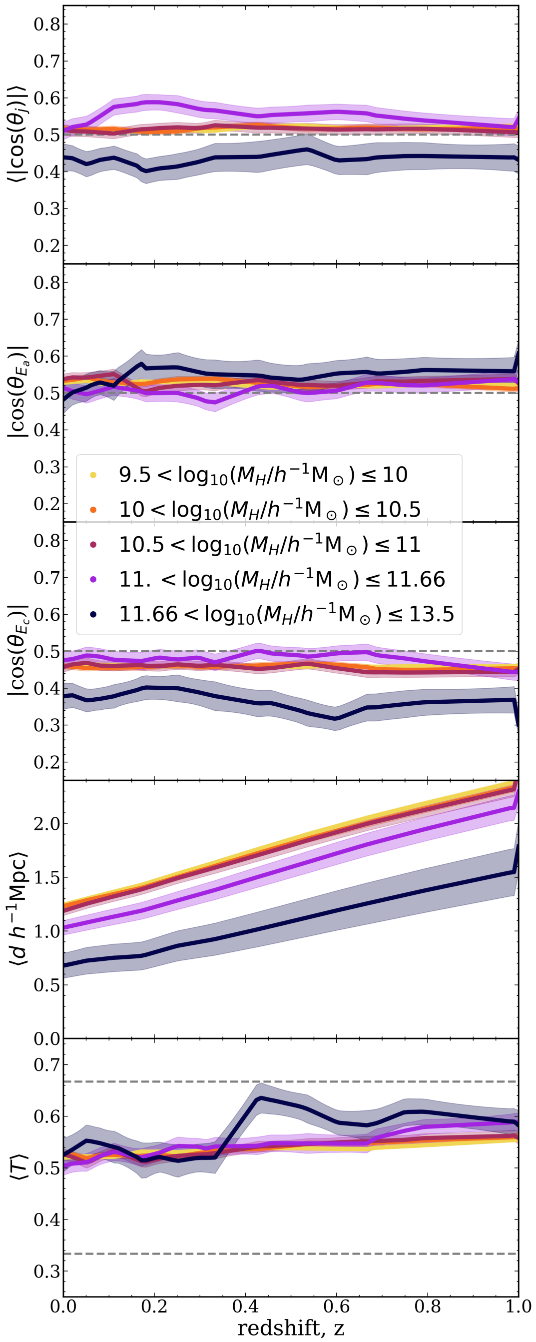

Figure 3.4: Average evolution of the halos belonging to the filaments at z=0 ($r \leq 3\ h^{-1}$Mpc), colored according to the final mass at $z = 0$, with shaded regions indicating the standard error of the mean. From top to bottom, the panels show the spin alignment with respect to the filament, the shape alignment of the major and minor axes with respect to the filament, the distance from the filament, and the triaxiality parameter T, respectively.

approaches redshift $z = 0$, while consistently maintaining a parallel trend. Instead of a progressive reorientation, the inertia tensor components display a trend of evolutionary invariance: the major axis remains consistently aligned parallel to the filament, while the minor axis maintains the perpendicular orientation established at high redshift, showing an almost unperturbed evolution. In contrast, the intermediate axis (not shown) remains statistically neutral (with alignment values around 0.5) throughout cosmic time. Consequently, we exclude it from further physical interpretation, as it appears to lack a dominant driving mechanism comparable to the stretching and compression acting on the other two axes.

Regarding the spatial distribution (fourth panel), we find a clear mass dependence. At $z = 0$, the most massive halos are preferentially located closer to the filament spine than low-mass halos. Since the mass bins are defined at $z = 0$, their progenitors are less massive at higher redshift, which should be kept in mind when interpreting the evolutionary trends. We also observe a mass-dependent trend in halo shape described by the triaxiality parameter (fifth panel). Halos in all mass bins (imposed at $z = 0$) evolve to become more spherical as cosmic time progresses. At $z = 1$ we see a more clear trend where massive halos exhibit more *prolate* shapes while low-mass halos are more *spherical*. This mass-dependent shape evolution is consistent with previous findings (e.g., Rossi et al., 2011). Finally, as redshift approaches $z = 1$, most curves tend to converge toward a common region, indicating a possible settling of these properties during halo evolution.

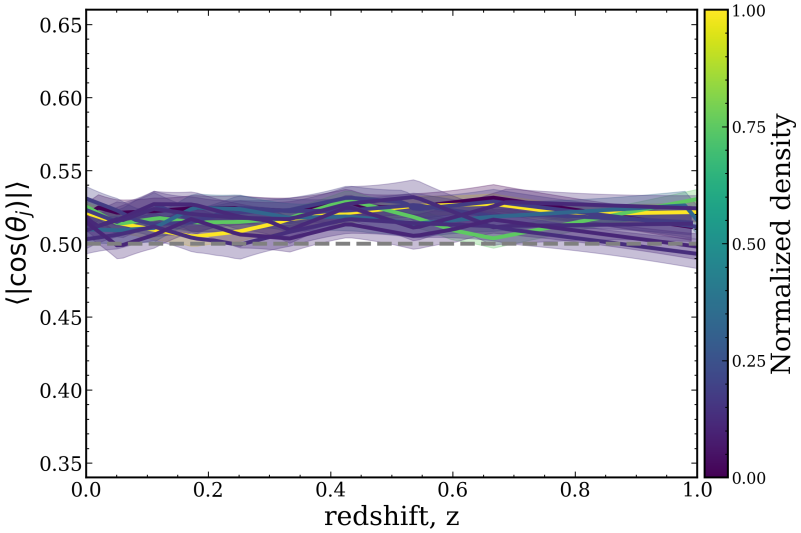

Figure 3.5: Average evolution of halos across the ten filaments. The curves are color-coded according to the particle number density reported in Table 2.1, normalized for visualization purposes.

Since we analyze a sample of ten filaments, one might expect variations in particle density to influence the alignment distributions. To test this, we examined the average evolution of halos within individual filaments (Figure 3.5) and found no significant differences in the alignment trends. This suggests that filament density does not strongly affect the overall behavior, reinforcing the conclusion that halo mass is the dominant factor, as shown in Figure 3.4. However, we note that the filaments in our sample have relatively similar densities, which may partly explain the lack of detectable variations.

3.3 Drivers of Spin Alignment

The angular momentum of DM halos originates primarily during the linear regime of structure formation, as described by TTT. To investigate the factors influencing its subsequent evolution in the non-linear regime, we categorize the halo population based on three distinct drivers: the history of spin–filament alignment, the distance to the host filament, and the time since the last major merger. Figures 3.6, 3.7, and 3.8 illustrate the average evolution of these subsets.

Given that halo mass plays a decisive role in the acquisition and redistribution of angular momentum, we further subdivide each subset into three mass bins defined at $z = 0$ to disentangle its effects: low ($9.5 \leq \log_{10}(M_h/h^{-1}\mathrm{M}_\odot) \leq 10.5$), intermediate ($10.5 < \log_{10}(M_h/h^{-1}\mathrm{M}_\odot) < 11.66$), and high mass ($\log_{10}(M_h/h^{-1}\mathrm{M}_\odot) \geq 11.66$). Additionally, we track the evolution of other relevant physical properties, such as the instantaneous halo mass and the spin parameter, λ'.

3.3.1 Subsampling by alignment evolution

Figure 3.6 presents the first classification, based on the type of alignment curve. We define four categories: *Neutral*, for halos that exhibit minimal variation in their alignment (fluctuations within ±0.2); *Positive*, defined by a consistent increase in alignment over time (i.e., evolving toward a parallel orientation); *Negative*, corresponding to halos that show a systematic decrease in alignment as redshift decreases; and *Varied*, which encompasses halos that do not fit into the previous categories. The *Varied* group is characterized by irregular or non-monotonic fluctuations that exceed the stability threshold but lack a directed trend.

Table 3.3: Number of halos by alignment curve and mass.

	Low-mass	Intermediate-mass	High-mass
Neutral	1013	169	7
Positive	526	84	6
Negative	574	89	10
Varied	2060	227	32

The number of halos in each category is listed in Table 3.3. Figure 3.6 shows the average evolution of several halo properties: spin–filament alignment, distance to the filament center, halo mass, triaxiality parameter, and spin parameter (from top to bottom, respectively). Each column, from left to right, corresponds to a different mass bin — low, intermediate, and high mass.

Examining the alignment tracks, we clearly distinguish the characteristic behaviors of the *Neutral*, *Positive*, *Negative*, and *Varied* categories. We observe a mass dependence: the downward shift of the curves becomes evident in the highest-mass bin, indicating that these halos tend to evolve toward perpendicular orientations relative to the filament. The *Neutral* curve generally lies slightly above the others in most mass bins, particularly in the two lower-mass bins. This tendency is more evident at certain redshifts and contributes, together with the *Positive* curve, to the population of halos exhibiting parallel orientations relative to the filament. Conversely, the *Negative* and *Varied* curves drive the perpendicular alignment signal observed at $z = 0$. The *Varied* curves remain close to the random alignment value of 0.5, typically lying slightly below

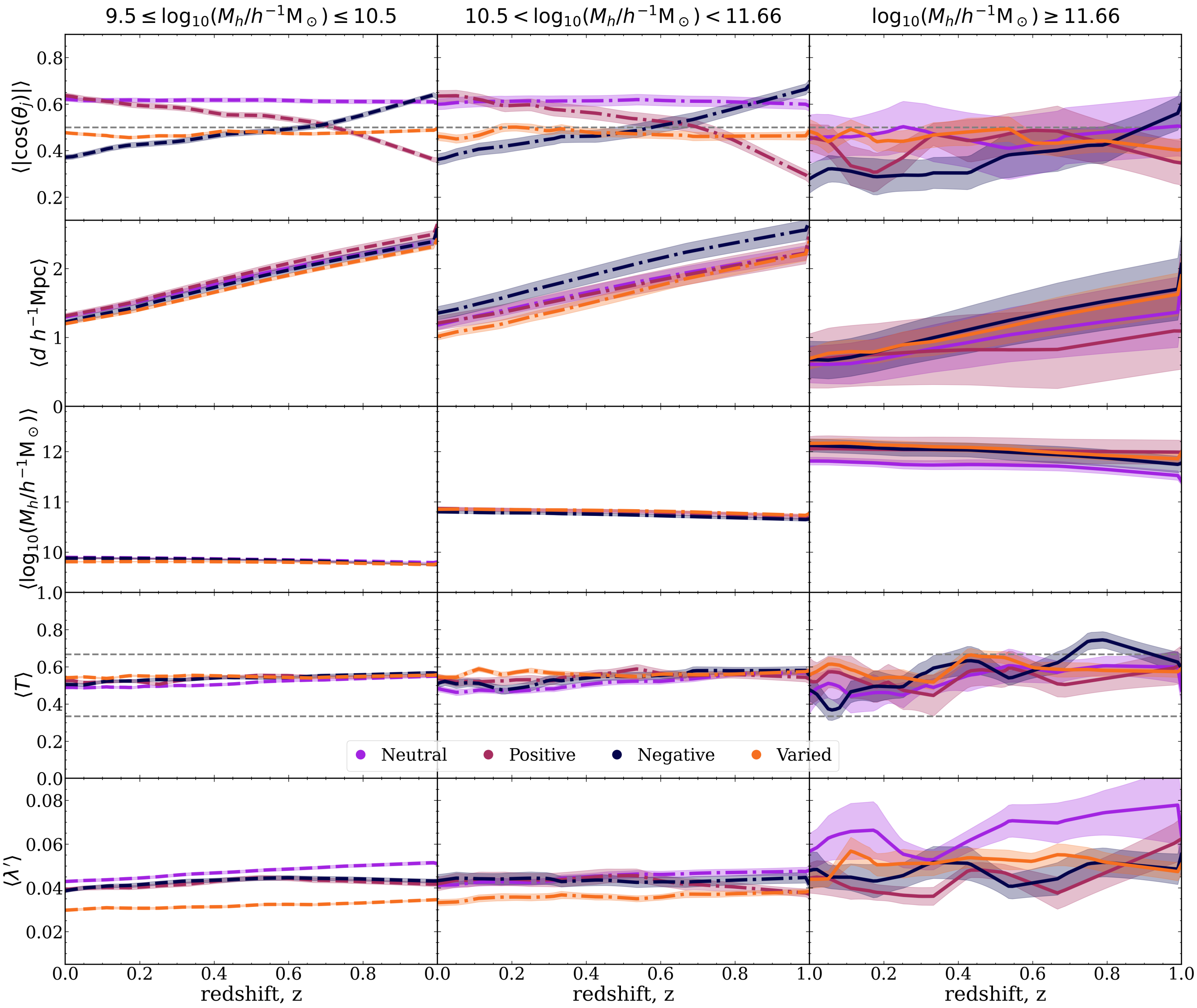

Figure 3.6: Similar to Figure 3.4, presents the evolution of halos grouped according to the type of alignment evolution curve they exhibit: black (*neutral*) for halos that do not experience significant changes, yellow (*positive*) for halos that become more parallel over time, red (*negative*) for halos showing a decrease in alignment, and orange (*varied*) for halos whose spin evolution does not fit into the previous three categories. Each column represents a different mass bin, arranged from left to right as follows: low mass ($9.5 \leq \log_{10.5}(M_h/h^{-1}\mathrm{M}_\odot) \leq 10$), intermediate mass ($10.5 < \log_{10}(M_h/h^{-1}\mathrm{M}_\odot) < 11.66$), and high mass ($\log_{10}(M_h/h^{-1}\mathrm{M}_\odot) \geq 11.66$).

it. This indicates that halos with erratic alignment histories do not exhibit a strong preferred orientation on average.

An additional insight emerges from the comparison between the different alignment classes. While halos classified as Negative dominate the population that ends up preferentially perpendicular to the filament in all mass bins, their average alignment histories exhibit a gradual drift toward misalignment. The perpendicular configuration may reflect the influence of additional physical processes beyond smooth tidal evolution. Such mechanisms could perturb the coherent alignment expected from linear theory. This behavior differs from the predictions of TTT, which anticipate a stable orientation inherited from the linear regime. In this context, halos with Neutral alignment histories provide a useful reference: across all mass bins, they follow similar evolutionary tracks and consistently remain more parallel to the filament, indicating that a relatively unperturbed evolution is broadly consistent with TTT. The deviation observed for halos ending in a perpendicular configuration may indicate the influence of nonlinear mass assembly, including anisotropic accretion along filaments and early interactions with the forming cosmic web. Such processes could reorient halo spins beyond the linear TTT prediction, in agreement with López et al. (2025). Given the redshift range explored here, we regard this interpretation as plausible but not definitive.

Regarding physical properties beyond alignment, such as the distance to the filament, we find no significant correlation with the alignment type. While there is a clear mass effect—more massive halos are located closer to the filament axis—the alignment history itself does not appear to dictate the halo's spatial position. As halo mass increases, the distance curves exhibit greater scatter without a consistent trend, a behavior likely driven by low-number statistics in the highest mass range. Similarly, the mass evolution tracks show no dependence on alignment type, reflecting only the expected growth for each mass bin. However, in terms of halo shape, we observe a slight difference: halos with a *Neutral* alignment history tend to be somewhat closer to oblate shapes ($T \to 0$), whereas those with *Varied* histories show a mild tendency toward more prolate configurations ($T \to 1$).

For the spin parameter λ', the trends are more distinguishable than for the shape. In the low-mass bins, halos with a *Neutral* alignment history tend to have slightly larger spin parameters compared to the other categories, while the *Varied* halos show marginally lower values of λ'. This difference is less evident in the high-mass bin. In the two lowest mass bins, these populations also tend to lie somewhat closer to the filament. Since this region is mildly denser and dynamically more complex, this spatial segregation may contribute to the lower spin values observed for the *Varied* halos, although this interpretation remains tentative.

3.3.2 Environmental dependence

Another potential driver of spin alignment is the environment within the filament. To investigate how different regions in the filament affect halo evolution, we classify halos based on their distance to the filament's center. Specifically, we define three environmental categories: halos that remain consistently within 1 h^{-1}Mpc, those located between 1 and 2 $^{-1}$Mpc, and those between 2 and 3 h^{-1}Mpc from the filament.

In Figure 3.7, we present the evolution of halos that remain in one of these distance-defined environments throughout their history, same as Figure 3.6 binned by mass, we also include an additional category labeled mixed, which contains halos that change environment over time and do not remain in a single region. The number of halos in each category is presented on Table 3.4.

The alignment evolves as expected for each mass bin when considering the distance. As indicated in Table 3.4, most of the population of massive halos remain closer to the filament throughout their evolution, which is associated with a strong perpendicular alignment trend. In contrast, halos in the lowest mass bin show alignments that are predominantly parallel to the filament, while those in the intermediate mass bin exhibit a qualitatively similar behavior, except in the 1–2 h^{-1}Mpc

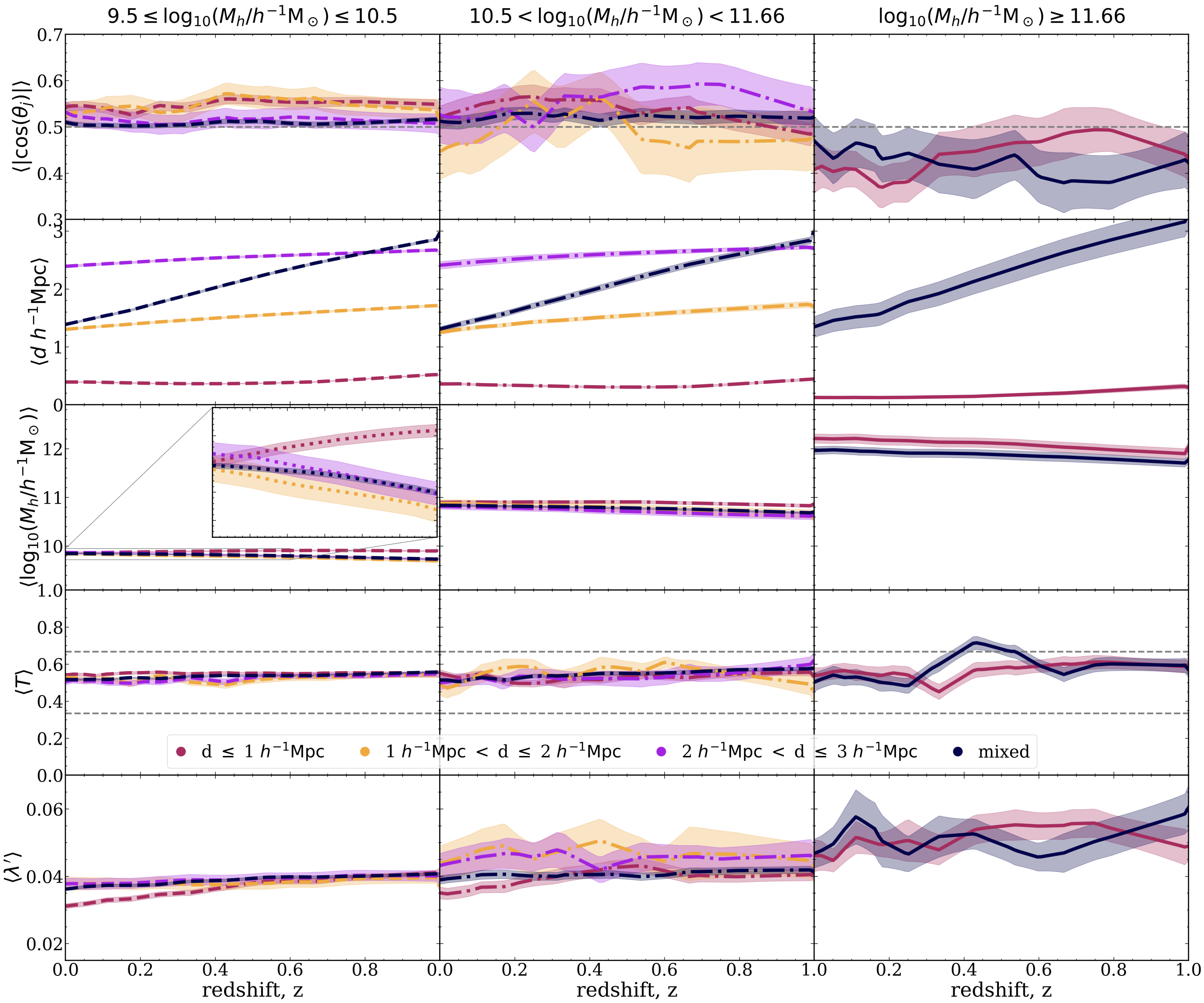

Figure 3.7: Same as Figure 3.6, but for the environment-based subsets. The curves are color-coded according to the distance d (in h^{-1}Mpc) from the halo to the filament center, as indicated in the legend. The category labeled 'mixed' includes halos that traverse multiple environments throughout their evolution.

Table 3.4: Number of halos by environment and mass.

	Low-mass	Intermediate-mass	High-mass
d $\leq 1\ h^{-1}$Mpc	785	125	31
$1-2\ h^{-1}$Mpc	146	18	0
$2-3\ h^{-1}$Mpc	181	25	1
Mixed	3061	401	23

range, where they tend to be more perpendicular to the filament.

There are no further comments regarding distance, as this is part of the selection criteria.

Besides that, halos in the highest-mass bin are predominantly located inside the filament, in contrast to the lower-mass bins where the mixed population dominates. Similar to Figure 3.6, only small differences with mass selection are visible. In the zoomed region, the lowest-mass bin shows a slight decrease in halos closest to the filament. However, this effect is minor and may be related to residual mass segregation within the bins or to mass growth with redshift. This is presumably because they are less strongly bound than massive halos, and interactions with the densest part of the filament lead to mass stripping. Additionally, the curves for the closest halos in the other two mass bins remain above the others, a result that was expected according to previous studies and is also shown in Figure 3.4.

Regarding shape, there is no distinctive trend driven by the environment. Finally, for the spin parameter, a decrease for the halos closest to the filaments is evident in the low- and intermediate-mass bins, whereas the highest-mass bin does not show a comparable trend. In the two lowest mass bins, the other two environments show higher spin values.

Motivated by the mass reduction observed in the halos closest to the filament ($d \leq 1\ h^{-1}$Mpc), we investigated whether mass stripping influences the alignment signal. For this analysis, we split the sample into two groups: those that have lost less than 25% of their initial mass and those that have lost more than 25% (not shown). Our analysis showed that mass loss, while affecting properties such as the distance to the filament and velocity, does not significantly alter the alignment signal. Therefore, we exclude these specific plots from the final results.

3.3.3 Subsampling by last major merger

Major mergers (hereafter MM) are widely known to produce significant changes in both galaxies and their host DM halos. In Figure 3.8, we present a classification based on the time since the last major merger (hereafter TSLMM), dividing the sample into five subsamples: halos whose last MM occurred at $z_{MM} \leq 0.25$, $0.25 < z_{MM} \leq 0.5$, $0.5 < z_{MM} \leq 0.75$, and $z_{MM} > 0.75$, as well as halos that have not undergone any MM. The distribution of these subsamples is listed in Table 3.5.

Table 3.5: Number of halos by TSLMM and mass.

	Low-mass	Intermediate-mass	High-mass
$z_{MM} \leq 0.25$	105	12	2
$0.25 < z_{MM} \leq 0.5$	83	3	2
$0.5 < z_{MM} \leq 0.75$	182	22	5
$z_{MM} > 0.75$	705	243	34
None	3098	289	12

As in the previous two plots, we use the same mass binning. In the high-mass bin, the effect of the last major merger is reflected in a change in alignment, with halos becoming either more parallel or more perpendicular to the filament. Halos that become perpendicular show a clearer connection with the merger time, whereas those that become parallel tend to evolve earlier and therefore do not exhibit an equally clear correlation. The subsample that exhibits an unperturbed evolution across all five panels corresponds to halos with $z_{MM} > 0.75$, which lie at high redshift and therefore not necessarily in the linear regime of interest. Despite the presence of halos that

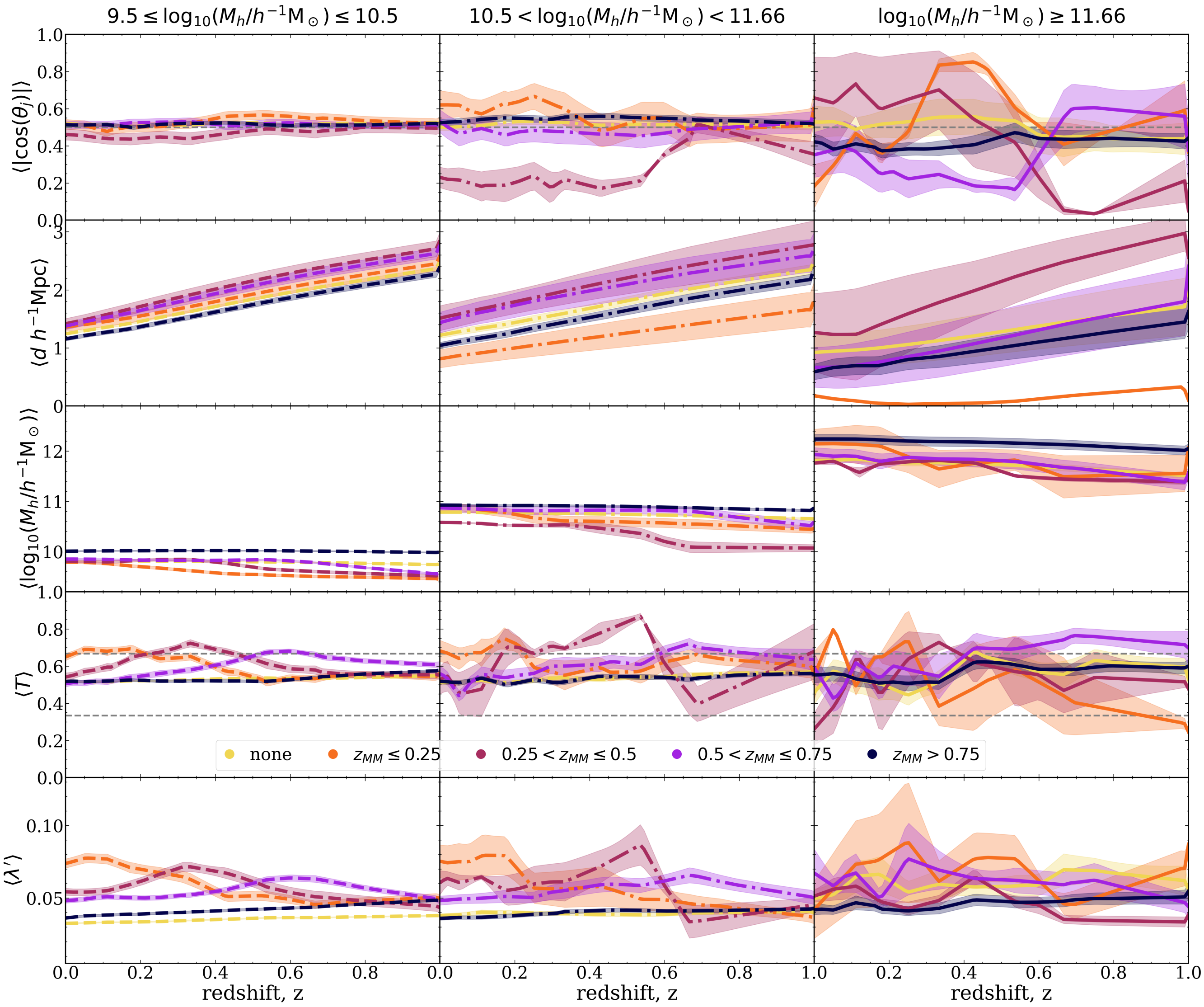

Figure 3.8: Same as Figure 3.6, but for the subsets based on the time since the last major merger (TSLMM). The curves are classified according to the redshift of the last event (z_{MM}), as indicated in the legend. The category labeled 'none' corresponds to halos that have not undergone a major merger.

have not undergone any major merger, most halos experienced such an event at high redshift, making major mergers in the nonlinear regime comparatively rare.

We also see a clear impact on mass growth: major mergers produce an increase in mass at the time of the event, consistently across the three mass bins. The shape evolution becomes especially interesting, as major mergers induce a temporary transition toward a more prolate configuration. Since these mergers typically occur along the major axis, the associated stretching modifies the halo's shape. Finally, the spin parameter is also affected by the merger, showing a noticeable increase at the time of the event. This behavior can be interpreted as a consequence of the accretion of orbital angular momentum during the major merger, coupled with a redistribution of the halo's kinetic and potential energy. Such events induce transient changes in the halo's internal structure, temporarily enhancing the relative contribution of ordered angular momentum to the system. This interpretation is consistent with our findings that, for early mergers, the post-merger increase in the spin parameter subsequently decays and stabilizes, indicating that these merger-induced effects are largely transient.

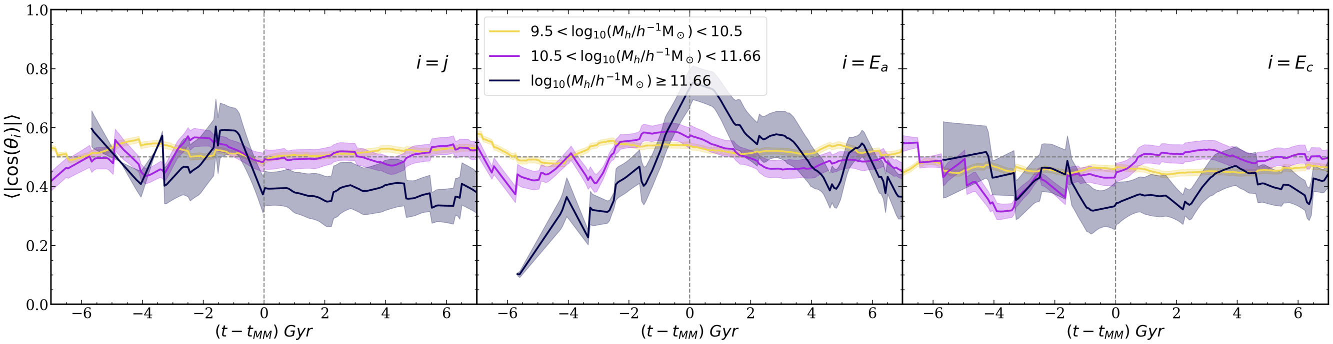

Figure 3.9: Average evolution of halos from the ten filaments, binned by mass, as a function of cosmic time relative to the last major merger. The top panel shows the evolution of the spin alignment, the middle panel shows the alignment of the major axis of the inertia tensor, and the bottom panel shows the alignment of the minor axis of the inertia tensor.

Given that major mergers have the strongest impact on alignment, we now investigate this effect in greater detail. Retaining the same mass binning, we shift from a static classification based on the time since the last merger to a dynamical analysis of the event itself. Figure 3.9 displays the evolution of the alignment of both the spin vector and the inertia tensor's principal axes with respect to the filament as a function of time relative to the merger epoch, defined such that the event occurs at $t = 0$.

The results demonstrate that major mergers induce a distinct reorientation across all three mass bins. For the spin vector, a decrease in alignment (i.e., a shift toward perpendicular orientation) becomes evident even prior to the merger event ($t < 0$), likely due to tidal pre-interaction. The strength of this signal diminishes with decreasing halo mass, becoming negligible for the lowest-mass bin. Regarding the inertia tensor, we observe a coherent response: the major axis alignment increases (becoming parallel to the filament) coincident with the spin becoming perpendicular. Conversely, the minor axis follows the spin's behavior, exhibiting a sharp drop in alignment. This trend is most pronounced in the high-mass bin.

These results are in agreement with previous works (e.g., Bett and Frenk, 2012, 2016), which found that major mergers produce significant changes in halo spin alignments. However, a nuanced interpretation is necessary. While our results confirm that major mergers cause the most dramatic individual reorientations (spin swings), they are relatively rare events. As noted by Bett and Frenk (2012), approximately 75% of significant spin changes are driven by the cumulative effect of minor mergers, accretion of small substructures, and flyby encounters, rather than by major mergers alone. Finally, regarding halo shape, major mergers drive the system toward a prolate configuration, effectively stretching the mass distribution along the merger axis, consistent with established models (Allgood et al., 2006).

In the context of MM recent work by Lee and Moon (2022) analyzed halos at $z = 0$ based on their latest merger epochs and did not find significant evidence for the effect of the last major merger on the global DM spin alignment with the large-scale tidal field. Consequently, they concluded that mergers are not the primary mechanism behind the mass-dependent spin transition. However, by dynamically tracking the evolution of halos relative to their specific merger times ($t - t_{MM}$), our results explicitly demonstrate that major mergers do induce strong, temporally localized reorientations of the spin vector relative to the filament.

3.4 Crosser Halos

Finally, we briefly address the dynamics of halos that cross the filament structure—specifically, those that travel from the outskirts, penetrate the filament core, and are subsequently expelled. To this end, we consider halos that are initially outside the filament at redshift $z = 1$, later enter the filament core—arbitrarily defined as a radius of $0.3, h^{-1},$Mpc around the filament center—and are subsequently expelled. For this analysis, we obtained very limited statistics, with a sample of only nine halos.

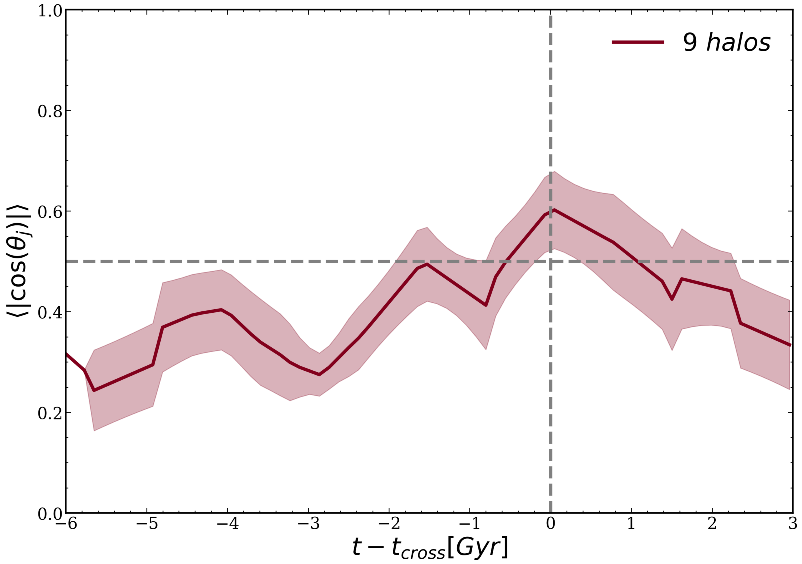

Figure 3.10: Average evolution of halos from the ten filaments as a function of cosmic time relative to the crossing time.

Figure 3.10 presents the average evolution of the spin alignment as a function of cosmic time relative to the crossing time, t_{cross}, of our sample of nine halos. We detect a strong signature in the spin alignment, suggesting that the filament environment can induce temporary modifications to the halo's dynamical state. This observation is consistent with the findings of Storck et al. (2024), who report a significant impact of non-linear environmental coupling. However, as the statistical sample of these specific crossing events is limited in our current simulation suite, we defer a detailed investigation of this phenomenon to future work.

Chapter 4

Discussion

Our results indicate that the evolution of halo spin alignment within filaments is primarily governed by the intrinsic, mass-dependent dynamical evolution of halos. In particular, the spin alignment measured at z=0 does not differ significantly from its value at earlier stages (z=1). This behavior is especially evident when halos are separated only by mass or by environment: in both cases, the average alignment curves show that halos tend to preserve their initial orientation. It is important to stress, however, that this behavior cannot be inferred from the subsampling by alignment evolution, since in that case halos are explicitly selected according to different alignment curves in order to investigate whether these behaviors are directly associated with other physical properties.

Major mergers, however, constitute a notable exception to this otherwise smooth evolutionary behavior. We find that mergers generate sharp and temporally localized reorientations of both the spin vector and the principal axes of the inertia tensor, accompanied by transient increases in the spin parameter and a shift toward more prolate shapes. These features are consistent with the interpretation that mergers inject orbital angular momentum into the remnant halo, which is subsequently redistributed during relaxation. Crucially, as shown by Welker et al. (2014), mergers preferentially occur along the direction of cosmic filaments. Consequently, the orbital angular momentum of the merging pair is oriented orthogonally to the filament axis. The conversion of this orbital momentum into the internal spin of the remnant drives the notable 'spin swings' we observe, effectively flipping the halo spin to a perpendicular configuration relative to the cosmic web. Since the most massive halos typically reside closer to the filament core, the deeper local potential well may enhance this coupling, amplifying the dynamical impact of mergers relative to halos in the outskirts.

The physical implications of our results extend naturally to galaxy formation. Several observational and theoretical studies have shown that the orientation of galactic disks and stellar angular momentum traces, at least partially, the angular-momentum content of their host halos (Hahn et al., 2007; Tempel and Libeskind, 2013). In this framework, our findings suggest that the intrinsic, mass-dependent halo evolution identified here provides the gravitational scaffold for the observed morphological dichotomy in galaxies, where low-mass spirals align parallel to filaments and massive ellipticals align perpendicularly (Welker et al., 2014; Kraljic et al., 2021).

Specifically, while major mergers act as a mechanism driving the perpendicular reorientation and 'spin swings' in massive systems Welker et al. (2014), the parallel alignment of low-mass halos is likely sustained by smooth accretion. As demonstrated by (Codis et al., 2012) and (Welker et al., 2014), unlike major mergers, the secular accretion of matter tends to build up specific angular momentum and re-align structures parallel to the filament, preserving the primordial vorticity imprint found in our Neutral and *Positive* evolutionary tracks.

However, a key distinction must be made regarding baryonic physics. While our dark-matter-only analysis shows that non-merging halos simply preserve their alignment, hydrodynamical simulations suggest that gas cooling can actively reform disks and re-align galaxies parallel to the filament over time, potentially competing with the perpendicular tendency driven by the halo (Welker et al., 2014; Jiang et al., 2019). A systematic comparison with hydrodynamical simulations will be required to quantify how these baryonic processes—such as feedback-driven outflows and disk instabilities—mediate or damp the imprint of the halo angular-momentum history on the observable galaxy population.

Chapter 5

Conclusions

In this work, we investigated the evolution of the spin alignments of DM halos within the non-linear regime of the cosmic web, focusing on ten zoom-in filaments. Our analysis shows that several features traditionally attributed to external influences—such as environmental effects or proximity to the filament core—are instead manifestations of the intrinsic, mass-driven evolution of halos. By separating the alignment curves, we observe that halos tend toward the characteristic orientation of their mass scale. Specifically, they transition from a parallel to a perpendicular regime as they grow in mass, with the exception of *Negative* halos, which remain perpendicular across all mass scales. Similarly, the filament environment itself does not introduce significant modifications to the alignment history: halos located inside, near, or outside the filament exhibit comparable evolutionary pathways, with mass consistently remaining the dominant factor.

In contrast, major mergers, although relatively rare, emerge as the process capable of producing a clear, coherent, and temporally localized impact on halo orientation, modifying the spin direction and altering the alignment of the inertia tensor. These results indicate that, within the non-linear regime, the dynamical history of halos—particularly mergers—plays a substantially greater role in determining spin alignment than the local filamentary environment. Our principal conclusions can be summarized as follows:

- Mass is the primary driver of spin–filament alignment. Low-mass halos tend to align parallel to filaments, whereas high-mass halos preferentially evolve toward perpendicular orientations, consistent with the canonical spin-flip behavior (Aragón-Calvo et al., 2007; Codis et al., 2012).
- Alignment curves reflect intrinsic halo evolution rather than external effects. Halos classified as *Neutral*, *Positive*, *Negative*, or *Varied*—representing approximately 25%, 13%, 14%, and 48% of the sample, respectively (considering the population selected according to the criteria defined in Section 3.2)—follow evolutionary paths primarily dictated by their mass, with no strong evidence for environmental modulation. An important insight emerging from this analysis is that *Neutral* halos consistently exhibit a more parallel alignment than the other classes, while *Negative* halos systematically evolve toward a more perpendicular configuration. This behavior supports the idea that the mechanisms driving perpendicular alignments require deviations from the predictions of TTT and predominantly arise in the non-linear regime (López et al., 2025).
- Analyzing our sample, we find that the filament environment does not significantly modify halo spin alignments; instead, halos largely preserve the alignment they acquired prior to

entering the filament. Grouping halos by fixed distance to the filament core reveals no substantial changes in the alignment evolution at fixed mass, reinforcing the dominance of halo mass over spatial location. Nevertheless, more massive halos are preferentially located closer to filament cores, implying that any apparent distance-dependent trend is largely driven by this mass segregation rather than by the filament environment itself.

- Major mergers constitute the strongest and most coherent driver of alignment changes. However, they remain relatively rare events in our simulation, with only ∼29% of halos experiencing at least one major merger over their lifetime (considering the population selected according to the criteria defined in Section 3.2). These events produce sharp reorientations of the spin vector, temporary transitions toward prolate shapes, and measurable increases in the spin parameter, with effects peaking near the merger time (Welker et al., 2014). We suggest that this pronounced effect is physically linked to a preferential direction of the mergers in the inside of the filament environment as this effect is enhanced for massive halos that are commonly in the inner regions of the filaments.

- The inertia tensor axes respond coherently to major mergers. In particular, as the spin becomes more perpendicular to the filament, the major axis tends to align with the filament, while the minor axis responds in a similar way to the spin alignment, exhibiting a progressively more perpendicular alignment signal toward the end of the evolution. This behavior is especially pronounced for the most massive halos (Bett and Frenk, 2012; Tenneti et al., 2014).

- In the non-linear regime, halo evolutionary history outweighs the large-scale environment. Once halos enter the non-linear phase, internal dynamical processes—especially mergers—induce the largest individual variations in alignment (Porciani et al., 2002a; Codis et al., 2015; Laigle et al., 2015). However, it is important to highlight that these events are not the main drivers of the overall misalignment statistics, which are dominated by the cumulative effect of minor interactions and accretion (Zavala et al., 2016; Ganeshaiah Veena et al., 2021).

Finally, we briefly explored additional dynamical scenarios capable of producing strong and rapid changes in spin alignment, such as so-called crosser halos. Although rare in our sample, halos that traverse the filament core exhibit transient enhancements in their alignment signal, indicating that filament crossing events can temporarily modify the dynamical state of halos. Given their low occurrence and the complexity of the associated dynamics, a detailed characterization of these systems is beyond the scope of the present work and is therefore deferred to a dedicated follow-up study.

Chapter 6

Future work

Looking ahead, several natural extensions of this work arise. First, our analysis is based on dark-matter-only simulations, and the inclusion of baryonic physics through hydrodynamical simulations will be essential to assess how gas cooling, star formation, and feedback processes modify halo spin acquisition and reorientation, particularly in the highly nonlinear regime explored here. Such effects are expected to be especially relevant for the inner regions of halos, where baryons can significantly reshape the angular momentum distribution (Dubois et al., 2014; Zavala et al., 2016; Kraljic et al., 2020).

A closely related aspect is the connection of our results with the framework of IA, i.e., coherent correlations in galaxy and halo orientations induced by large-scale tidal fields, which constitute both a probe of structure formation and a major astrophysical systematic in cosmological analyses (Hirata and Seljak, 2004; Troxel and Ishak, 2015, see Chisari 2025 for a complete review). Intrinsic alignments can significantly bias cosmological parameter inference from weak lensing and clustering measurements, and can also affect cross-correlations with other probes such as CMB lensing if not properly modeled (Hikage et al., 2019; Fabbian et al., 2019). While hydrodynamical simulations already show that galaxy spins and shapes exhibit mass- and environment-dependent alignments with the local tidal field (Chisari et al., 2015), our results indicate that halo spin–filament alignment is mainly governed by halo mass and internal dynamical history. In particular, non-linear events such as major mergers produce the strongest localized reorientations, pointing to a picture in which IA originate from early tidal imprints but are subsequently reshaped by non-linear evolution, including mergers and anisotropic accretion. This highlights the importance of incorporating realistic, mass-dependent and non-linear evolutionary pathways, such as those identified in this work, into IA models aimed at interpreting current and future cosmological data.

Finally, the trends identified here open promising avenues for comparison with upcoming large-scale surveys. Observational programs such as Euclid (Mellier et al., 2025) and the Vera C. Rubin Observatory (LSST, LSST Science Collaboration et al., 2009) will provide unprecedented constraints on galaxy orientations, shapes, and their relation to the cosmic web. Establishing a robust connection between halo spin alignments in simulations and observable galaxy properties will be a key step toward testing these theoretical predictions in a cosmological context.

Bibliography

Allgood, B., Flores, R. A., Primack, J. R., Kravtsov, A. V., Wechsler, R. H., Faltenbacher, A., and Bullock, J. S. (2006). The shape of dark matter haloes: dependence on mass, redshift, radius and formation. , 367(4):1781–1796.

Aragón-Calvo, M. A., van de Weygaert, R., Jones, B. J. T., and van der Hulst, J. M. (2007). Spin Alignment of Dark Matter Halos in Filaments and Walls. , 655(1):L5–L8.

Aragon-Calvo, M. A. and Yang, L. F. (2014). The hierarchical nature of the spin alignment of dark matter haloes in filaments. , 440:L46–L50.

Awad, P., Peletier, R., Canducci, M., Smith, R., Taghribi, A., Mohammadi, M., Shin, J., Tiňo, P., and Bunte, K. (2023). Swarm-intelligence-based extraction and manifold crawling along the large-scale structure. *Monthly Notices of the Royal Astronomical Society*, 520(3):4517–4539.

Bailin, J. and Steinmetz, M. (2005). Internal and external alignment of the shapes and angular momenta of cdm halos. *The Astrophysical Journal*, 627(2):647–665.

Bett, P. E. and Frenk, C. S. (2012). Spin flips – i. evolution of the angular momentum orientation of milky way-mass dark matter haloes. *Monthly Notices of the Royal Astronomical Society*, 420(4):3324–3333.

Bett, P. E. and Frenk, C. S. (2016). Spin flips – ii. evolution of dark matter halo spin orientation, and its correlation with major mergers. *Monthly Notices of the Royal Astronomical Society*, 461(2):1338–1355.

Bonamigo, M., Despali, G., Limousin, M., Angulo, R., Giocoli, C., and Soucail, G. (2015). Universality of dark matter haloes shape over six decades in mass: insights from the Millennium XXL and SBARBINE simulations. , 449(3):3171–3182.

Bond, J. R., Kofman, L., and Pogosyan, D. (1996). How filaments of galaxies are woven into the cosmic web. , 380(6575):603–606.

Borzyszkowski, M. R. (2018). *The large-scale structure of the Universe; environmental effects and relativistic corrections*. PhD thesis, Rheinische Friedrich Wilhelms University of Bonn, Germany.

Bullock, J. S., Dekel, A., Kolatt, T. S., Kravtsov, A. V., Klypin, A. A., Porciani, C., and Primack, J. R. (2001). A universal angular momentum profile for galactic halos. *The Astrophysical Journal*, 555(1):240.

Butsky, I., Macciò, A. V., Dutton, A. A., Wang, L., Obreja, A., Stinson, G. S., Penzo, C., Kang, X., Keller, B. W., and Wadsley, J. (2016). NIHAO project II: halo shape, phase-space density and velocity distribution of dark matter in galaxy formation simulations. , 462(1):663–680.

Canducci, M., Awad, P., Taghribi, A., Mohammadi, M., Mastropietro, M., De Rijcke, S., Peletier, R., Smith, R., Bunte, K., and Tiňo, P. (2022). 1-dream: 1d recovery, extraction and analysis of manifolds in noisy environments. *Astronomy and Computing*, 41:100658.

Chisari, N., Codis, S., Laigle, C., Dubois, Y., Pichon, C., Devriendt, J., Slyz, A., Miller, L., Gavazzi, R., and Benabed, K. (2015). Intrinsic alignments of galaxies in the Horizon-AGN cosmological hydrodynamical simulation. , 454(3):2736–2753.

Chisari, N. E. (2025). A rising tide: intrinsic alignments since the turn of the millennium. , 33(1):5.

Codis, S., Jindal, A., Chisari, N. E., Vibert, D., Dubois, Y., Pichon, C., and Devriendt, J. (2018). Galaxy orientation with the cosmic web across cosmic time. , 481(4):4753–4774.

Codis, S., Pichon, C., Devriendt, J., Slyz, A., Pogosyan, D., Dubois, Y., and Sousbie, T. (2012). Connecting the cosmic web to the spin of dark haloes: implications for galaxy formation. *Monthly Notices of the Royal Astronomical Society*, 427(4):3320–3336.

Codis, S., Pichon, C., and Pogosyan, D. (2015). Spin alignments within the cosmic web: a theory of constrained tidal torques near filaments. *Monthly Notices of the Royal Astronomical Society*, 452(4):3369–3393.

Doroshkevich, A. G. (1970). Spatial structure of perturbations and origin of galactic rotation in fluctuation theory. *Astrophysics*, 6(4):320–330.

Dubois, Y., Pichon, C., Welker, C., Le Borgne, D., Devriendt, J., Laigle, C., Codis, S., Pogosyan, D., Arnouts, S., Benabed, K., Bertin, E., Blaizot, J., Bouchet, F., Cardoso, J.-F., Colombi, S., de Lapparent, V., Desjacques, V., Gavazzi, R., Kassin, S., Kimm, T., McCracken, H., Milliard, B., Peirani, S., Prunet, S., Rouberol, S., Silk, J., Slyz, A., Sousbie, T., Teyssier, R., Tresse, L., Treyer, M., Vibert, D., and Volonteri, M. (2014). Dancing in the dark: galactic properties trace spin swings along the cosmic web. *Monthly Notices of the Royal Astronomical Society*, 444(2):1453–1468.

Fabbian, G., Lewis, A., and Beck, D. (2019). CMB lensing reconstruction biases in cross-correlation with large-scale structure probes. , 2019(10):057.

Faltenbacher, A., Kerscher, M., Gottloeber, S., and Mueller, V. (2002). Correlations in the orientations of galaxy clusters. *Astron. Astrophys.*, 395:1–10.

Forero-Romero, J. E., Contreras, S., and Padilla, N. (2014). Cosmic web alignments with the shape, angular momentum and peculiar velocities of dark matter haloes. , 443(2):1090–1102.

Ganeshaiah Veena, P., Cautun, M., van de Weygaert, R., Tempel, E., and Frenk, C. S. (2021). Cosmic ballet iii: Halo spin evolution in the cosmic web. *Monthly Notices of the Royal Astronomical Society*, 503(2):2280–2299.

Ganeshaiah Veena, P., Cautun, M., van de Weygaert, R., Tempel, E., Jones, B. J. T., Rieder, S., and Frenk, C. S. (2018). The cosmic ballet: spin and shape alignments of haloes in the cosmic web. *Monthly Notices of the Royal Astronomical Society*, 481(1):414–438.

Hahn, O. and Abel, T. (2011). Multi-scale initial conditions for cosmological simulations: Multi-scale initial conditions. *Monthly Notices of the Royal Astronomical Society*, 415(3):2101–2121.

Hahn, O., Porciani, C., Carollo, C. M., and Dekel, A. (2007). Properties of dark matter haloes in clusters, filaments, sheets and voids. *Monthly Notices of the Royal Astronomical Society*, 375(2):489–499.

Hatton, S. and Ninin, S. (2001). Angular momentum alignment of dark matter haloes. , 322(3):576–584.

Hayashi, E., Navarro, J. F., and Springel, V. (2007). The shape of the gravitational potential in cold dark matter haloes. , 377(1):50–62.

Hikage, C., Oguri, M., Hamana, T., More, S., Mandelbaum, R., Takada, M., Köhlinger, F., Miyatake, H., Nishizawa, A. J., Aihara, H., Armstrong, R., Bosch, J., Coupon, J., Ducout, A., Ho, P., Hsieh, B.-C., Komiyama, Y., Lanusse, F., Leauthaud, A., Lupton, R. H., Medezinski, E., Mineo, S., Miyama, S., Miyazaki, S., Murata, R., Murayama, H., Shirasaki, M., Sifón, C., Simet, M., Speagle, J., Spergel, D. N., Strauss, M. A., Sugiyama, N., Tanaka, M., Utsumi, Y., Wang, S.-Y., and Yamada, Y. (2019). Cosmology from cosmic shear power spectra with Subaru Hyper Suprime-Cam first-year data. , 71(2):43.

Hirata, C. M. and Seljak, U. (2004). Intrinsic alignment-lensing interference as a contaminant of cosmic shear. , 70(6):063526.

Hirv, A., Pelt, J., Saar, E., Tago, E., Tamm, A., Tempel, E., and Einasto, M. (2017). Alignment of galaxies relative to their local environment in sdss-dr8. *AA*, 599:A31.

Hoyle, F. (1951). The Origin of the Rotations of the Galaxies. In *Problems of Cosmical Aerodynamics*, page 195.

Huchra, J. P. and Geller, M. J. (1982). Groups of Galaxies. I. Nearby groups. , 257:423–437.

Jiang, F., Dekel, A., Kneller, O., Lapiner, S., Ceverino, D., Primack, J. R., Faber, S. M., Macciò, A. V., Dutton, A. A., Genel, S., and Somerville, R. S. (2019). Is the dark-matter halo spin a predictor of galaxy spin and size? , 488(4):4801–4815.

Jing, Y. P. and Suto, Y. (2002). Triaxial Modeling of Halo Density Profiles with High-Resolution N-Body Simulations. , 574(2):538–553.

Jones, B. J. T., van de Weygaert, R., and Aragón-Calvo, M. A. (2010). Fossil evidence for spin alignment of sloan digital sky survey galaxies in filaments. *Monthly Notices of the Royal Astronomical Society*, 408(2):897–918.

Kasun, S. F. and Evrard, A. E. (2005). Shapes and Alignments of Galaxy Cluster Halos. , 629(2):781–790.

Knollmann, S. R. and Knebe, A. (2009). AHF: Amiga's Halo Finder. , 182(2):608–624.

Kraljic, K., Davé, R., and Pichon, C. (2020). And yet it flips: connecting galactic spin and the cosmic web. , 493(1):362–381.

Kraljic, K., Duckworth, C., Tojeiro, R., Alam, S., Bizyaev, D., Weijmans, A.-M., Boardman, N. F., and Lane, R. R. (2021). Sdss-iv manga: 3d spin alignment of spiral and s0 galaxies. *Monthly notices of the Royal Astronomical Society*, 504(3):4626–4633.

Krolewski, A., Ho, S., Chen, Y.-C., Chan, P. F., Tenneti, A., Bizyaev, D., and Kraljic, K. (2019). Alignment between filaments and galaxy spins from the manga integral-field survey. *The Astrophysical Journal*, 876(1):52.

Laigle, C., Pichon, C., Codis, S., Dubois, Y., Le Borgne, D., Pogosyan, D., Devriendt, J., Peirani, S., Prunet, S., Rouberol, S., Slyz, A., and Sousbie, T. (2015). Swirling around filaments: are large-scale structure vortices spinning up dark haloes? , 446(3):2744–2759.

Lee, J. and Moon, J.-S. (2022). Merger Effects on the Spin and Shape Alignments of Galaxy Stellar, Cold Gas, Hot Gas, and Dark Matter Components. , 936(2):119.

Lee, J. and Pen, U.-L. (2001). Galaxy Spin Statistics and Spin-Density Correlation. , 555(1):106–124.

Libeskind, N. I., Hoffman, Y., Forero-Romero, J., Gottlöber, S., Knebe, A., Steinmetz, M., and Klypin, A. (2013). The velocity shear tensor: tracer of halo alignment. , 428(3):2489–2499.

López, P., Merchán, M. E., and Paz, D. J. (2019). Deviations from tidal torque theory: environment dependences on halo angular momentum growth. , 485(4):5244–5255.

López, P., van de Weygaert, R., and Merchán, M. (2025). Spinning masters: on the impact of tidal forces and protohalo size on early spin evolution. , 543(3):2222–2242.

LSST Science Collaboration, Abell, P. A., Allison, J., Anderson, S. F., Andrew, J. R., Angel, J. R. P., Armus, L., Arnett, D., Asztalos, S. J., Axelrod, T. S., and et al. (2009). LSST Science Book, Version 2.0. *ArXiv e-prints*.

López, P., Cautun, M., Paz, D., Merchán, M., and van de Weygaert, R. (2021). Deviations from tidal torque theory: Evolution of the halo spin–filament alignment. *Monthly Notices of the Royal Astronomical Society*, 502(4):5528–5545.

Mellier, Y., Abdurro'uf, Acevedo Barroso, J. A., Achúcarro, A., Adamek, J., Adam, R., Addison, G. E., Aghanim, N., Aguena, M., Ajani, V., Akrami, Y., Al-Bahlawan, A., Alavi, A., Albuquerque, I. S., Alestas, G., Alguero, G., Allaoui, A., Allen, S. W., Allevato, V., Alonso-Tetilla, A. V., Altieri, B., Alvarez-Candal, A., Alvi, S., Amara, A., Amendola, L., Amiaux, J., Andika, I. T., Andreon, S., Andrews, A., Angora, G., Angulo, R. E., Annibali, F., Anselmi, A., Anselmi, S., Arcari, S., Archidiacono, M., Aricò, G., Arnaud, M., Arnouts, S., Asgari, M., Asorey, J., Atayde, L., Atek, H., Atrio-Barandela, F., Aubert, M., Aubourg, E., Auphan, T., Auricchio, N., Aussel, B., Aussel, H., Avelino, P. P., Avgoustidis, A., Avila, S., Awan, S., Azzollini, R., Baccigalupi, C., Bachelet, E., Bacon, D., Baes, M., Bagley, M. B., Bahr-Kalus, B., Balaguera-Antolinez, A., Balbinot, E., Balcells, M., Baldi, M., Baldry, I., Balestra, A., Ballardini, M., Ballester, O., Balogh, M., Bañados, E., Barbier, R., Bardelli, S., Baron, M., Barreiro, T., Barrena, R., Barriere, J.-C., Barros, B. J., Barthelemy, A., Bartolo, N., Basset, A., Battaglia, P., Battisti, A. J., Baugh, C. M., Baumont, L., Bazzanini, L., Beaulieu, J.-P., Beckmann, V., Belikov, A. N., Bel, J., Bellagamba, F., Bella, M., Bellini, E., Benabed, K., Bender, R., Benevento, G., Bennett, C. L., Benson, K., Bergamini, P., Bermejo-Climent, J. R., Bernardeau, F., Bertacca, D., Berthe, M., Berthier, J., Bethermin, M., Beutler, F., Bevillon, C., Bhargava, S., Bhatawdekar, R., Bianchi, D., Bisigello, L., Biviano, A., Blake, R. P., Blanchard, A., Blazek, J., Blot, L., Bosco, A., Bodendorf, C., Boenke, T., Böhringer, H., Boldrini, P., Bolzonella, M., Bonchi, A., Bonici, M., Bonino, D., Bonino, L., Bonvin, C., Bon, W., Booth, J. T., Borgani, S., Borlaff, A. S., Borsato, E., Bosco, A., Bose, B., Botticella, M. T., Boucaud, A., Bouche, F., Boucher, J. S., Boutigny, D., Bouvard, T., Bouwens, R., Bouy, H., Bowler, R. A. A., Bozza, V., Bozzo, E., Branchini, E., Brando, G., Brau-Nogue, S., Brekke, P., Bremer, M. N., Brescia, M., Breton, M.-A., Brinchmann, J., Brinckmann, T., Brockley-Blatt, C., Brodwin, M., Brouard, L., Brown, M. L., Bruton, S., Bucko, J., Buddelmeijer, H., Buenadicha, G., Buitrago, F., Burger, P., Burigana, C., Busillo, V., Busonero, D., Cabanac, R., Cabayol-Garcia, L., Cagliari, M. S., Caillat, A., Caillat, L., Calabrese, M., Calabro, A., Calderone, G., Calura, F., Camacho Quevedo, B., Camera, S., Campos, L., Cañas-Herrera, G., Candini, G. P., Cantiello, M., Capobianco, V., Cappellaro, E., Cappelluti, N., Cappi, A., Caputi, K. I., Cara, C., Carbone, C., Cardone, V. F., Carella, E., Carlberg, R. G., Carle, M., Carminati, L., Caro, F., Carrasco, J. M., Carretero, J., Carrilho, P., Carron Duque, J., Carry, B., Carvalho, A., Carvalho, C. S., Casas, R., Casas, S., Casenove, P., Casey, C. M., Cassata, P., Castander, F. J., Castelao, D., Castellano, M., Castiblanco, L., Castignani, G., Castro, T., Cavet, C., Cavuoti, S., Chabaud, P.-Y., Chambers, K. C., Charles, Y., Charlot, S., Chartab, N., Chary, R., Chaumeil, F., Cho, H., Chon, G., Ciancetta, E., Ciliegi, P., Cimatti, A., Cimino, M., Cioni, M.-R. L., Claydon, R., Cleland, C., Clément, B., Clements, D. L., Clerc, N., Clesse, S., Codis, S., Cogato, F., Colbert, J., Cole, R. E., Coles, P., Collett, T. E., Collins, R. S., Colodro-Conde, C., Colombo, C., Combes, F., Conforti, V., Congedo, G., Conseil, S., Conselice, C. J., Contarini, S., Contini, T., Conversi, L., Cooray, A. R., Copin, Y., Corasaniti, P.-S., Corcho-Caballero, P., Corcione, L., Cordes, O., Corpace, O., Correnti, M., Costanzi, M., Costille, A., Courbin, F., Courcoult Mifsud, L., Courtois, H. M., Cousinou, M.-C., Covone, G., Cowell, T., Cragg, C., Cresci, G., Cristiani, S., Crocce, M., Cropper, M., Crouzet, P. E., Csizi, B., Cuby, J.-G., Cucchetti, E., Cucciati, O., Cuillandre, J.-C., Cunha, P. A. C., Cuozzo, V., Daddi, E., D'Addona, M., Dafonte, C., Dagoneau, N., Dalessandro, E., Dalton, G. B., D'Amico, G., Dannerbauer, H., Danto, P., Das, I., Da Silva, A., da Silva, R., d'Assignies Doumerg, W., Daste, G., Davies, J. E., Davini, S., Dayal, P., de Boer, T., Decarli, R., De Caro, B., Degaudenzi, H., Degni, G., de Jong, J. T. A., de la Bella, L. F., de la Torre, S., Delhaise, F., Delley, D., Delucchi, G., De Lucia, G., Denniston, J., De Paolis, F., De Petris, M., Derosa, A., Desai, S., Desjacques, V., Despali, G., Desprez, G., De Vicente-Albendea, J., Deville, Y., Dias, J. D. F., Díaz-Sánchez, A., Diaz, J. J., Di Domizio, S., Diego, J. M., Di Ferdinando, D., Di Giorgio, A. M., Dimauro, P., Dinis, J., Dolag, K., Dolding, C., Dole, H., Domínguez Sánchez, H., Doré, O., Dournac, F., Douspis, M., Dreihahn, H., Droge, B., Dryer, B., Dubath, F., Duc, P.-A., Ducret, F., Duffy, C., Dufresne, F., Duncan, C. A. J., Dupac, X., Duret, V., Durrer, R., Durret, F., Dusini, S., Ealet, A., Eggemeier, A., Eisenhardt, P. R. M., Elbaz, D., Elkhashab, M. Y., Ellien, A., Endicott, J., Enia, A., Erben, T., Escartin Vigo, J. A., Escoffier, S., Escudero Sanz, I., Essert, J., Ettori, S., Ezziati, M., Fabbian, G., Fabricius, M., Fang, Y., Farina, A., Farina, M., Farinelli, R., Farrens, S., Faustini, F., Feltre, A., Ferguson, A. M. N., Ferrando, P., Ferrari, A. G., Ferré-Mateu, A., Ferreira, P. G., Ferreras, I., Ferrero, I., Ferriol, S., Ferruit, P., Filleul, D., Finelli, F., Finkelstein, S. L., Finoguenov, A., Fiorini, B., Flentge, F., Focardi, P., Fonseca, J., Fontana, A., Fontanot, F., Fornari, F., Fosalba, P., Fossati, M., Fotopoulou, S., Fouchez, D., Fourmanoit, N., Frailis, M., Fraix-Burnet, D., Franceschi, E., Franco, A., Franzetti, P., Freihoefer, J., Frenk, C. S., Frittoli, G., Frugier, P.-A., Frusciante, N., Fumagalli, A., Fumagalli, M., Fumana, M., Fu, Y., Gabarra, L., Galeotta, S., Galluccio, L., Ganga, K., Gao, H., García-Bellido, J., Garcia, K., Gardner, J. P., Garilli, B., Gaspar-Venancio, L.-M., Gasparetto, T., Gautard, V., Gavazzi, R., Gaztanaga, E., Genolet, L., Genova Santos, R., Gentile, F., George, K., Gerbino, M., Ghaffari, Z., Giacomini, F., Gianotti, F., Gibb, G. P. S., Gillard, W., Gillis, B., Ginolfi, M., Giocoli, C., Girardi, M., Giri, S. K., Goh, L. W. K., Gómez-Alvarez, P., Gonzalez-Perez, V., Gonzalez, A. H., Gonzalez, E. J., Gonzalez, J. C., Gouyou Beauchamps, S., Gozaliasl, G., Gracia-Carpio, J., Grandis, S., Granett, B. R., Granvik, M., Grazian, A., Gregorio, A., Grenet, C., Grillo, C., Grupp, F., Gruppioni, C., Gruppuso, A., Guerbuez, C., Guerrini, S., Guidi, M., Guillard, P., Gutierrez, C. M., Guttridge, P., Guzzo, L., Gwyn, S., Haapala, J., Haase, J., Haddow, C. R., Hailey, M., Hall, A., Hall, D., Hamaus, N., Haridasu, B. S., Harnois-Déraps, J., Harper, C., Hartley, W. G., Hasinger, G., Hassani, F., Hatch, N. A., Haugan, S. V. H., Häußler, B., Heavens, A., Heisenberg, L., Helmi, A., Helou, G., Hemmati, S., Henares, K., Herent, O., Hernández-Monteagudo, C., Heuberger, T., Hewett, P. C., Heydenreich, S., Hildebrandt, H., Hirschmann, M., Hjorth, J., Hoar, J., Hoekstra, H., Holland, A. D., Holliman, M. S., Holmes, W., Hook, I., Horeau, B., Hormuth, F., Hornstrup, A., Hosseini, S., Hu, D., Hudelot, P., Hudson, M. J., Huertas-Company, M., Huff, E. M., Hughes, A. C. N., Humphrey, A., Hunt, L. K., Huynh, D. D., Ibata, R., Ichikawa, K., Iglesias-Groth, S., Ilbert, O., Ilić, S., Ingoglia, L., Iodice, E., Israel, H., Israelsson, U. E., Izzo, L., Jablonka, P., Jackson, N., Jacobson, J., Jafariyazani, M., Jahnke, K., Jain, B., Jansen, H., Jarvis, M. J., Jasche, J., Jauzac, M., Jeffrey, N., Jhabvala, M., Jimenez-Teja, Y., Jimenez Muñoz, A., Joachimi, B., Johansson, P. H., Joudaki, S., Jullo, E., Kajava, J. J. E., Kang, Y., Kannawadi, A., Kansal, V., Karagiannis, D., Kärcher, M., Kashlinsky, A., Kazandjian, M. V., Keck, F., Keihänen, E., Kerins, E., Kermiche, S., Khalil, A., Kiessling, A., Kiiveri, K., Kilbinger, M., Kim, J., King, R., Kirkpatrick, C. C., Kitching, T., Kluge, M., Knabenhans, M., Knapen, J. H., Knebe, A., Kneib, J.-P., Kohley, R., Koopmans, L. V. E., Koskinen, H., Koulouridis, E., Kou, R., Kovács, A., Kovačić, I., Kowalczyk, A., Koyama, K., Kraljic, K., Krause, O., Kruk, S., Kubik, B., Kuchner, U., Kuijken, K., Kümmel, M., Kunz, M., Kurki-Suonio, H., Lacasa, F., Lacey, C. G., La Franca, F., Lagarde, N., Lahav, O., Laigle, C., La Marca, A., La Marle, O., Lamine, B., Lam, M. C., Lançon, A., Landt, H., Langer, M., Lapi, A., Larcheveque, C., Larsen, S. S., Lattanzi, M., Laudisio, F., Laugier, D., Laureijs, R., Laurent, V., Lavaux, G., Lawrenson, A., Lazanu, A., Lazeyras, T., Le Boulc'h, Q., Le Brun, A. M. C., Le Brun, V., Leclercq, F., Lee, S., Le Graet, J., Legrand, L., Leirvik, K. N., Le Jeune, M., Lembo, M., Le Mignant, D., Lepinzan, M. D., Lepori, F., Le Reun, A., Leroy, G., Lesci, G. F., Lesgourgues, J., Leuzzi, L., Levi, M. E., Liaudat, T. I., Libet, G., Liebing, P., Ligori, S., Lilje, P. B., Lin, C.-C., Linde, D., Linder, E., Lindholm, V., Linke, L., Li, S.-S., Liu, S. J., Lloro, I., Lobo, F. S. N., Lodieu, N., Lombardi, M., Lombriser, L., Lonare, P., Longo, G., López-Caniego, M., Lopez Lopez, X., Lorenzo Alvarez, J., Loureiro, A., Loveday, J., Lusso, E., Macias-Perez, J., Maciaszek, T., Maggio, G., Magliocchetti, M., Magnard, F., Magnier, E. A., Magro, A., Mahler, G., Mainetti, G., Maino, D., Maiorano, E., Maiorano, E., Malavasi, N., Mamon, G. A., Mancini, C., Mandelbaum, R., Manera, M., Manjón-García, A., Mannucci, F., Mansutti, O., Manteiga Outeiro, M., Maoli, R., Maraston, C., Marcin, S., Marcos-Arenal, P., Margalef-Bentabol, B., Marggraf, O., Marinucci, D., Marinucci, M., Markovic, K., Marleau, F. R., Marpaud, J., Martignac, J., Martín-Fleitas, J., Martin-Moruno, P., Martin, E. L., Martinelli, M., Martinet, N., Martin, H., Martins, C. J. A. P., Marulli, F., Massari, D., Massey, R., Masters, D. C., Matarrese, S., Matsuoka, Y., Matthew, S., Maughan, B. J., Mauri, N., Maurin, L., Maurogordato, S., McCarthy, K., McConnachie, A. W., McCracken, H. J., McDonald, I., McEwen, J. D., McPartland, C. J. R., Medinaceli, E., Mehta, V., Mei, S., Melchior, M., Melin, J.-B., Ménard, B., Mendes, J., Mendez-Abreu, J., Meneghetti, M., Mercurio, A., Merlin, E., Metcalf, R. B., Meylan, G., Migliaccio, M., Mignoli, M., Miller, L., Miluzio, M., Milvang-Jensen, B., Mimoso, J. P., Miquel, R., Miyatake, H., Mobasher, B., Mohr, J. J., Monaco, P., Monguió, M., Montoro, A., Mora, A., Moradinezhad Dizgah, A., Moresco, M., Moretti, C., Morgante, G., Morisset, N., Moriya, T. J., Morris, P. W., Mortlock, D. J., Moscardini, L., Mota, D. F., Mottet, S., Moustakas, L. A., Moutard, T., Müller, T., Munari, E., Murphree, G., Murray, C., Murray, N., Musi, P., Nadathur, S., Nagam, B. C., Nagao, T., Naidoo, K., Nakajima, R., Nally, C., Natoli, P., Navarro-Alsina, A., Navarro Girones, D., Neissner, C., Nersesian, A., Nesseris, S., Nguyen-Kim, H. N., Nicastro, L., Nichol, R. C., Nielbock, M., Niemi, S.-M., Nieto, S., Nilsson, K., Noller, J., Norberg, P., Nouri-Zonoz, A., Ntelis, P., Nucita, A. A., Nugent, P., Nunes, N. J., Nutma, T., Ocampo, I., Odier, J., Oesch, P. A., Oguri, M., Magalhaes Oliveira, D., Onoue, M., Oosterbroek, T., Oppizzi, F., Ordenovic, C., Osato, K., Pacaud, F., Pace, F., Padilla, C., Paech, K., Pagano, L., Page, M. J., Palazzi, E., Paltani, S., Pamuk, S., Pandolfi, S., Paoletti, D., Paolillo, M., Papaderos, P., Pardede, K., Parimbelli, G., Parmar, A., Partmann, C., Pasian, F., Passalacqua, F., Paterson, K., Patrizii, L., Pattison, C., Paulino-Afonso, A., Paviot, R., Peacock, J. A., Pearce, F. R., Pedersen, K., Peel, A., Peletier, R. F., Pellejero Ibanez, M., Pello, R., Penny, M. T., Percival, W. J., Perez-Garrido, A., Perotto, L., Pettorino, V., Pezzotta, A., Pezzuto, S., Philippon, A., Pierre, M., Piersanti, O., Pietroni, M., Piga, L., Pilo, L., Pires, S., Pisani, A., Pizzella, A., Pizzuti, L., Plana, C., Polenta, G., Pollack, J. E., Poncet, M., Pöntinen, M., Pool, P., Popa, L. A., Popa, V., Popp, J., Porciani, C., Porth, L., Potter, D., Poulain, M., Pourtsidou, A., Pozzetti, L., Prandoni, I., Pratt, G. W., Prezelus, S., Prieto, E., Pugno, A., Quai, S., Quilley, L., Racca, G. D., Raccanelli, A., Rácz, G., Radinović, S., Radovich, M., Ragagnin, A., Ragnit, U., Raison, F., Ramos-Chernenko, N., Ranc, C., Rasera, Y., Raylet, N., Rebolo, R., Refregier, A., Reimberg, P., Reiprich, T. H., Renk, F., Renzi, A., Retre, J., Revaz, Y., Reylé, C., Reynolds, L., Rhodes, J., Ricci, F., Ricci, M., Riccio, G., Ricken, S. O., Rissanen, S., Risso, I., Rix, H.-W., Robin, A. C., Rocca-Volmerange, B., Rocci, P.-F., Rodenhuis, M., Rodighiero, G., Rodriguez Monroy, M., Rollins, R. P., Romanello, M., Roman, J., Romelli, E., Romero-Gomez, M., Roncarelli, M., Rosati, P., Rosset, C., Rossetti, E., Roster, W., Rottgering, H. J. A., Rozas-Fernández, A., Ruane, K., Rubino-Martin, J. A., Rudolph, A., Ruppin, F., Rusholme, B., Sacquegna, S., Sáez-Casares, I., Saga, S., Saglia, R., Sahlén, M., Saifollahi, T., Sakr, Z., Salvalaggio, J., Salvaterra, R., Salvati, L., Salvato, M., Salvignol, J.-C., Sánchez, A. G., Sanchez, E., Sanders, D. B., Sapone, D., Saponara, M., Sarpa, E., Sarron, F., Sartori, S., Sartoris, B., Sassolas, B., Sauniere, L., Sauvage, M., Sawicki, M., Scaramella, R., Scarlata, C., Scharré, L., Schaye, J., Schewtschenko, J. A., Schindler, J.-T., Schinnerer, E., Schirmer, M., Schmidt, F., Schmidt, F., Schmidt, M., Schneider, A., Schneider, M., Schneider, P., Schöneberg, N., Schrabback, T., Schultheis, M., Schulz, S., Schuster, N., Schwartz, J., Sciotti, D., Scodeggio, M., Scognamiglio, D., Scott, D., Scottez, V., Secroun, A., Sefusatti, E., Seidel, G., Seiffert, M., Sellentin, E., Selwood, M., Semboloni, E., Sereno, M., Serjeant, S., Serrano, S., Setnikar, G., Shankar, F., Sharples, R. M., Short, A., Shulevski, A., Shuntov, M., Sias, M., Sikkema, G., Silvestri, A., Simon, P., Sirignano, C., Sirri, G., Skottfelt, J., Slezak, E., Sluse, D., Smith, G. P., Smith, L. C., Smith, R. E., Smit, S. J. A., Soldano, F., Solheim, B. G. B., Sorce, J. G., Sorrenti, F., Soubrie, E., Spinoglio, L., Spurio Mancini, A., Stadel, J., Stagnaro, L., Stanco, L., Stanford, S. A., Starck, J.-L., Stassi, P., Steinwagner, J., Stern, D., Stone, C., Strada, P., Strafella, F., Stramaccioni, D., Surace, C., Sureau, F., Suyu, S. H., Swindells, I., Szafraniec, M., Szapudi, I., Taamoli, S., Talia, M., Tallada-Crespí, P., Tanidis, K., Tao, C., Tarrío, P., Tavagnacco, D., Taylor, A. N., Taylor, J. E., Taylor, P. L., Teixeira, E. M., Tenti, M., Teodoro Idiago, P., Teplitz, H. I., Tereno, I., Tessore, N., Testa, V., Testera, G., Tewes, M., Teyssier, R., Theret, N., Thizy, C., Thomas, P. D., Toba, Y., Toft, S., Toledo-Moreo, R., Tolstoy, E., Tommasi, E., Torbaniuk, O., Torradeflot, F., Tortora, C., Tosi, S., Tosti, S., Trifoglio, M., Troja, A., Trombetti, T., Tronconi, A., Tsedrik, M., Tsyganov, A., Tucci, M., Tutusaus, I., Uhlemann, C., Ulivi, L., Urbano, M., Vacher, L., Vaillon, L., Valageas, P., Valdes, I., Valentijn, E. A., Valenziano, L., Valieri, C., Valiviita, J., Van den Broeck, M., Vassallo, T., Vavrek, R., Vega-Ferrero, J., Venemans, B., Venhola, A., Ventura, S., Verdoes Kleijn, G., Vergani, D., Verma, A., Vernizzi, F., Veropalumbo, A., Verza, G., Vescovi, C., Vibert, D., Viel, M., Vielzeuf, P., Viglione, C., Viitanen, A., Villaescusa-Navarro, F., Vinciguerra, S., Visticot, F., Voggel, K., von Wietersheim-Kramsta, M., Vriend, W. J., Wachter, S., Walmsley, M., Walth, G., Walton, D. M., Walton, N. A., Wander, M., Wang, L., Wang, Y., Weaver, J. R., Weller, J., Wetzstein, M., Whalen, D. J., Whittam, I. H., Widmer, A., Wiesmann, M., Wilde, J., Williams, O. R., Winther, H.-A., Wittje, A., Wong, J. H. W., Wright, A. H., Yankelevich, V., Yeung, H. W., Yoon, M., Youles, S., Yung, L. Y. A., Zacchei, A., Zalesky, L., Zamorani, G., Zamorano Vitorelli, A., Zanoni Marc, M., Zennaro, M., Zerbi, F. M., Zinchenko, I. A., Zoubian, J., Zucca, E., and Zumalacarregui, M. (2025). Euclid: I. overview of the euclid mission. *Astronomy amp; Astrophysics*, 697:A1.

Padmanabhan, T. (1993). *Structure Formation in the Universe.*

Peebles, P. J. E. (1969). Origin of the Angular Momentum of Galaxies. , 155:393.

Peebles, P. J. E. (1980). *The large-scale structure of the universe.*

Pichon, C., Codis, S., Pogosyan, D., Dubois, Y., Desjacques, V., and Devriendt, J. (2014). Why do galactic spins flip in the cosmic web? a theory of tidal torques near saddles. *Proceedings of the International Astronomical Union*, 11(S308):421–432.

Planck Collaboration, Aghanim, N., Akrami, Y., Ashdown, M., Aumont, J., Baccigalupi, C., Ballardini, M., Banday, A. J., Barreiro, R. B., Bartolo, N., Basak, S., Battye, R., Benabed, K., Bernard, J.-P., Bersanelli, M., Bielewicz, P., Bock, J. J., Bond, J. R., Borrill, J., Bouchet, F. R., Boulanger, F., Bucher, M., Burigana, C., Butler, R. C., Calabrese, E., Cardoso, J.-F., Carron, J., Challinor, A., Chiang, H. C., Chluba, J., Colombo, L. P. L., Combet, C., Contreras, D., Crill, B. P., Cuttaia, F., de Bernardis, P., de Zotti, G., Delabrouille, J., Delouis, J.-M., Di Valentino, E., Diego, J. M., Doré, O., Douspis, M., Ducout, A., Dupac, X., Dusini, S., Efstathiou, G., Elsner, F., Enßlin, T. A., Eriksen, H. K., Fantaye, Y., Farhang, M., Fergusson, J., Fernandez-Cobos, R., Finelli, F., Forastieri, F., Frailis, M., Fraisse, A. A., Franceschi, E., Frolov, A., Galeotta, S., Galli, S., Ganga, K., Génova-Santos, R. T., Gerbino, M., Ghosh, T., González-Nuevo, J., Górski, K. M., Gratton, S., Gruppuso, A., Gudmundsson, J. E., Hamann, J., Handley, W., Hansen, F. K., Herranz, D., Hildebrandt, S. R., Hivon, E., Huang, Z., Jaffe, A. H., Jones, W. C., Karakci, A., Keihänen, E., Keskitalo, R., Kiiveri, K., Kim, J., Kisner, T. S., Knox, L., Krachmalnicoff, N., Kunz, M., Kurki-Suonio, H., Lagache, G., Lamarre, J.-M., Lasenby, A., Lattanzi, M., Lawrence, C. R., Le Jeune, M., Lemos, P., Lesgourgues, J., Levrier, F., Lewis, A., Liguori, M., Lilje, P. B., Lilley, M., Lindholm, V., López-Caniego, M., Lubin, P. M., Ma, Y.-Z., Macías-Pérez, J. F., Maggio, G., Maino, D., Mandolesi, N., Mangilli, A., Marcos-Caballero, A., Maris, M., Martin, P. G., Martinelli, M., Martínez-González, E., Matarrese, S., Mauri, N., McEwen, J. D., Meinhold, P. R., Melchiorri, A., Mennella, A., Migliaccio, M., Millea, M., Mitra, S., Miville-Deschênes, M.-A., Molinari, D., Montier, L., Morgante, G., Moss, A., Natoli, P., Nørgaard-Nielsen, H. U., Pagano, L., Paoletti, D., Partridge, B., Patanchon, G., Peiris, H. V., Perrotta, F., Pettorino, V., Piacentini, F., Polastri, L., Polenta, G., Puget, J.-L., Rachen, J. P., Reinecke, M., Remazeilles, M., Renzi, A., Rocha, G., Rosset, C., Roudier, G., Rubiño-Martín, J. A., Ruiz-Granados, B., Salvati, L., Sandri, M., Savelainen, M., Scott, D., Shellard, E. P. S., Sirignano, C., Sirri, G., Spencer, L. D., Sunyaev, R., Suur-Uski, A.-S., Tauber, J. A., Tavagnacco, D., Tenti, M., Toffolatti, L., Tomasi, M., Trombetti, T., Valenziano, L., Valiviita, J., Van Tent, B., Vibert, L., Vielva, P., Villa, F., Vittorio, N., Wandelt, B. D., Wehus, I. K., White, M., White, S. D. M., Zacchei, A., and Zonca, A. (2020). Planck 2018 results - vi. cosmological parameters. *AA*, 641:A6.

Porciani, C., Dekel, A., and Hoffman, Y. (2002a). Testing tidal-torque theory - I. Spin amplitude and direction. , 332(2):325–338.

Porciani, C., Dekel, A., and Hoffman, Y. (2002b). Testing tidal-torque theory - II. Alignment of inertia and shear and the characteristics of protohaloes. , 332(2):339–351.

Prada, J., Forero-Romero, J. E., Grand, R. J. J., Pakmor, R., and Springel, V. (2019). Dark matter halo shapes in the Auriga simulations. , 490(4):4877–4888.

Press, W. H. and Schechter, P. (1974). Formation of galaxies and clusters of galaxies by selfsimilar gravitational condensation. *Astrophys. J.*, 187:425–438.

Raj, M. A., Awad, P., Peletier, R. F., Smith, R., Kuchner, U., van de Weygaert, R., Libeskind, N. I., Canducci, M., Tiňo, P., and Bunte, K. (2024). Large-scale structure around the Fornax-Eridanus complex. , 690:A92.

Rossi, G., Sheth, R. K., and Tormen, G. (2011). Modelling the shapes of the largest gravitationally bound objects. , 416(1):248–261.

Shao, S., Cautun, M., Frenk, C. S., Gao, L., Crain, R. A., Schaller, M., Schaye, J., and Theuns, T. (2016). Alignments between galaxies, satellite systems and haloes. *Monthly Notices of the Royal Astronomical Society*, 460(4):3772–3783.

Sousbie, T., Colombi, S., and Pichon, C. (2009). The fully connected n-dimensional skeleton: probing the evolution of the cosmic web. *Monthly Notices of the Royal Astronomical Society*, 393(2):457–477.

Storck, A., Cadiou, C., Agertz, O., and Galárraga-Espinosa, D. (2024). The causal effect of cosmic filaments on dark matter halos.

Tempel, E. and Libeskind, N. I. (2013). Galaxy spin alignment in filaments and sheets: Observational evidence. *The Astrophysical Journal Letters*, 775(2):L42.

Tempel, E., Stoica, R. S., and Saar, E. (2012). Evidence for spin alignment of spiral and elliptical/s0 galaxies in filaments. *Monthly Notices of the Royal Astronomical Society*, 428(2):1827–1836.

Tenneti, A., Mandelbaum, R., Di Matteo, T., Feng, Y., and Khandai, N. (2014). Galaxy shapes and intrinsic alignments in the MassiveBlack-II simulation. , 441(1):470–485.

Teyssier, R. (2002). Cosmological hydrodynamics with adaptive mesh refinement. A new high resolution code called RAMSES. , 385:337–364.

Troxel, M. A. and Ishak, M. (2015). The intrinsic alignment of galaxies and its impact on weak gravitational lensing in an era of precision cosmology. , 558:1–59.

Velliscig, M., Cacciato, M., Schaye, J., Crain, R. A., Bower, R. G., van Daalen, M. P., Dalla Vecchia, C., Frenk, C. S., Furlong, M., McCarthy, I. G., Schaller, M., and Theuns, T. (2015). The alignment and shape of dark matter, stellar, and hot gas distributions in the EAGLE and cosmo-OWLS simulations. , 453(1):721–738.

Vera-Ciro, C. A., Sales, L. V., Helmi, A., Frenk, C. S., Navarro, J. F., Springel, V., Vogelsberger, M., and White, S. D. M. (2011). The shape of dark matter haloes in the Aquarius simulations: evolution and memory. , 416(2):1377–1391.

Welker, C., Devriendt, J., Dubois, Y., Pichon, C., and Peirani, S. (2014). Mergers drive spin swings along the cosmic web. *Monthly Notices of the Royal Astronomical Society: Letters*, 445(1):L46–L50.

White, S. D. M. (1984). Angular momentum growth in protogalaxies. , 286:38–41.

Zavala, J., Frenk, C. S., Bower, R., Schaye, J., Theuns, T., Crain, R. A., Trayford, J. W., Schaller, M., and Furlong, M. (2016). The link between the assembly of the inner dark matter halo and the angular momentum evolution of galaxies in the eagle simulation. *Monthly Notices of the Royal Astronomical Society*, 460(4):4466–4482.

Zel'dovich, Y. B. (1970). Gravitational instability: An approximate theory for large density perturbations. , 5:84–89.

Zhang, Y., Yang, X., Faltenbacher, A., Springel, V., Lin, W., and Wang, H. (2009). The spin and orientation of dark matter halos within cosmic filaments. *The Astrophysical Journal*, 706(1):747.

Zhang, Y., Yang, X., Wang, H., Wang, L., Luo, W., Mo, H. J., and van den Bosch, F. C. (2014). Spin alignments of spiral galaxies within the large-scale structure from sdss dr7. *The Astrophysical Journal*, 798(1):17.

Zhang, Y., Yang, X., Wang, H., Wang, L., Mo, H. J., and van den Bosch, F. C. (2013). Alignments of galaxies within cosmic filaments from sdss dr7. *The Astrophysical Journal*, 779(2):160.